Development of structures under the influence of heterogeneous flow field around rigid inclusions: insights from theoretical and numerical models

Susanta Kumar Samanta [a], Nibir Mandal [a], Chandan Chakraborty [b,*]

[a] *Department of Geological Sciences, Jadavpur University, Calcutta 700032, India*
[b] *Geological Studies Unit, Indian Statistical Institute, 203 B.T. Road, Calcutta 700035, India*

Abstract

Rocks that are mechanically heterogeneous due to the presence of stiff or rigid inclusions floating in a ductile matrix, commonly show a variety of micro- to macro-scale structures developing under the influence of heterogeneous flow field in the neighbourhood of the inclusions. It is of fundamental importance to apprehend the nature of strain heterogeneity around inclusions to understand progressive development of structures associated with rigid inclusions such as strain shadow, foliation drag, porphyroclast mantle, porphyroblast inclusion trails, intragranular fractures, etc. The development of these diverse types of structures can be analyzed with the help of a suitable hydrodynamic theory. In this paper, we review different continuum models that have been proposed to characterize the heterogeneous flow field around rigid inclusions, focusing on recent developments. Recent studies reveal that Jeffery's [Proc. R. Soc. Lond. A 120 (1922) 161.] theory dealing with the motion of ellipsoidal rigid bodies in an infinitely extended viscous medium is more general in nature, and applicable for modeling the heterogeneous flow around both equant and inequant shapes of inclusions and ideal or non-ideal shear deformation of the matrix. The application of this theory, therefore, has advantages over other models, based on Lamb's [Lamb, H., 1932. Hydrodynamics. Cambridge University Press, Cambridge.] theory dealing with spherical inclusions. The review finally illustrates numerical simulations based on hydrodynamic theories, highlighting the controls of physical and kinematic factors on the progressive development of the structures mentioned above.

Keywords: flow field; drag patterns; mantle structure; inclusion trails; intragranular fractures

1. Introduction

Deformation of a rock system characterized by stiff or rigid inclusions floating in a ductile matrix produces a variety of micro- to macro-scale structures under the influence of heterogeneous flow field around the inclusions. In rocks the rigid inclusions are usually represented by stiff, large mineral grains (porphyroblasts or porphyroclasts), xenoliths, pebbles etc., and the related geological structures include foliation drag, strain shadows, porphyroclast tails, porphyroblast inclusion trails and intragranular fractures (Fig. 1). All these structures are common in deformed rocks and are useful kinematic indicators. It is therefore essential to understand the mechanics of formation of the aforesaid structures for their precise and proper application in the kinematic analysis of deformed rocks.

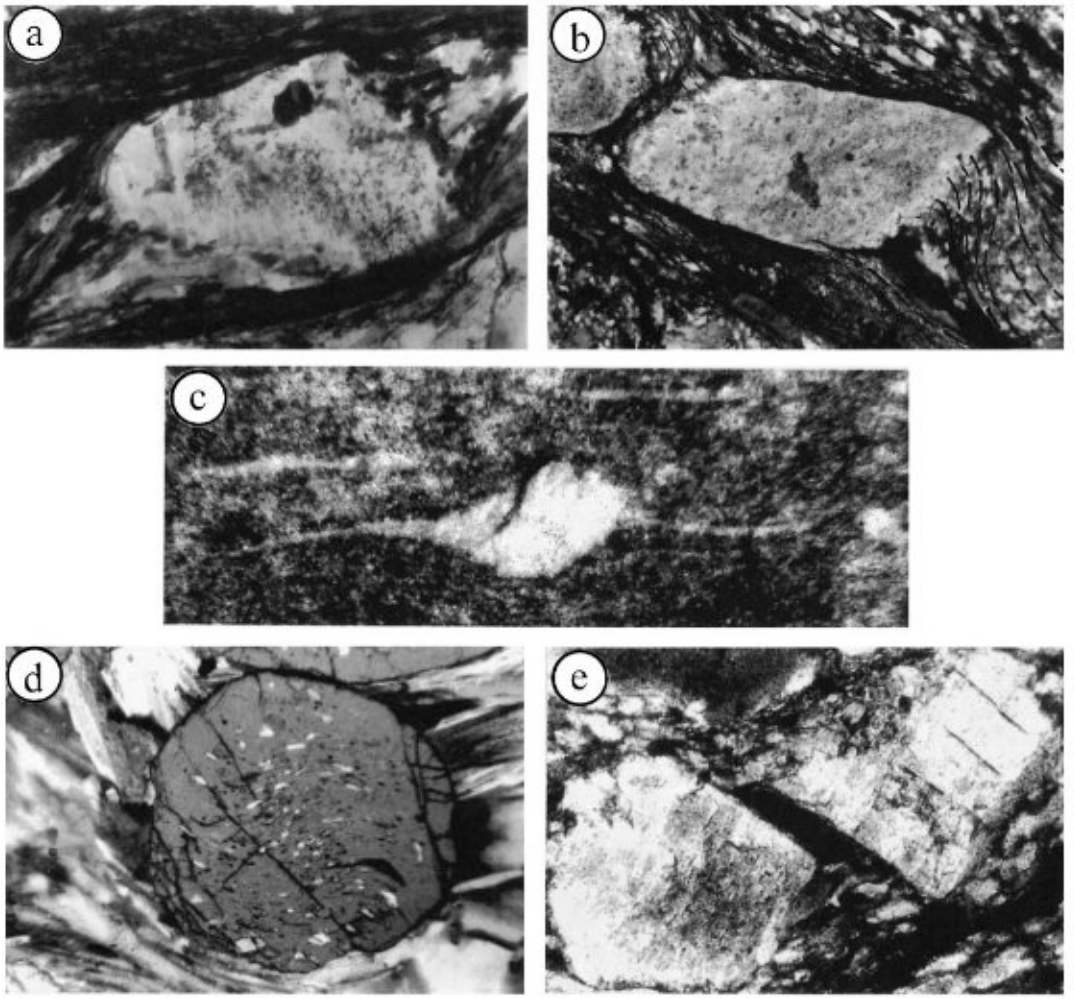

Fig. 1. Natural examples of different types of structures associated with rigid inclusions: (a) strain shadow, (b) foliation drag, (c) porphyroclast tails, (d) porphyroblast inclusion trails, (e) intragranular fractures. (a), (b), (d) and (e) are photomicrographs. (c) is a field photograph.

In structural geology the kinematics of stiff but deformable, and rigid inclusions embedded within a ductile matrix has been a subject of study over several decades (Gay, 1968; Reed and Tryggvason, 1974; Ghosh and Ramberg, 1976; Ferguson, 1979; Freeman, 1985; Fernandez, 1987; Passchier, 1987; Masuda et al., 1995; Jezek et al., 1996). These analyses mostly concentrate on how the floating inclusions change their shape or rotate bodily in the course of progressive deformation, but do not really focus on the consequences of the heterogeneous flow field in the matrix induced by the stiff inclusions. Understandably, the heterogeneous flow field around stiff inclusions is crucial to model structures, such as foliation drag, strain shadow etc. Using numerical and analog models some workers have attempted analysis of heterogeneous deformation in the matrix (Ghosh and Sengupta, 1973; Masuda and Ando, 1988; Mandal and Chakraborty, 1990; Ildefonse et al., 1992; Ildefonse and Mancktelow, 1993; Masuda and Mizuno, 1995, 1996a,b; Kenkmann and Dresen, 1998; Pennacchioni et al., 2000). The studies using this approach led to a better understanding of many kinematically important

structures, such as foliation drag patterns, inclusion trail patterns of porphyroblasts and mantle structures around porphyroclasts.

The heterogeneous flow field that rigid inclusions induce in their neighborhood also influences the nature of brittle deformation of inclusions that may result in response to the traction exerted on them by the flowing matrix (Hobbs, 1967; Lloyd and Ferguson, 1981; Lloyd et al., 1982; Hancock, 1985; Ramsay and Huber, 1987; Masuda and Kuriyama, 1988; Hippertt, 1993; Michibayashi, 1996; Ji and Zhao, 1993; Ji et al., 1997). Considering the stress transfer from the flowing matrix to the matrix-inclusion interface (shear-lag model), several workers (Ramberg, 1955; Hobbs, 1967; Lloyd et al., 1982; Pollard and Segall, 1987; Masuda and Kuriyama, 1988; Mandal et al., 1994; Ji et al., 1997) have analyzed the mechanism of fracturing of brittle grains embedded in a softer matrix under a bulk pure shear deformation.

In this review, we first present a detailed account of different theoretical formulations that derive the velocity functions in order to characterize the heterogeneous flow of the matrix and rotation of the inclusion. The next section describes different numerical models that have been developed using the velocity functions to understand: (1) the nature of particle paths in the matrix; (2) the development of strain shadow zones and distortion patterns of passive foliations around an inclusion; and (3) the mantle structures around porphyroclasts and inclusion trails within porphyroblasts. Lastly, the paper describes different theoretical and experimental studies that have considered the effects of heterogeneous flow around inclusions on the development of intragranular fractures.

2. Velocity field around rigid inclusions

2.1. Theoretical formulations

Different continuum models have been formulated to analyze the deformation of a matrix-inclusion system, based on elastic or viscous rheology of the matrix. Considering elastic rheology and using plane theory of elasticity (Muskhelishvilli, 1953), several workers have analyzed the kinematics of stiff inclusions floating in a softer matrix and the neighboring strain field (Eshelby, 1957, 1959; Ghosh and Sengupta, 1973; Mandal and Chakraborty, 1990; Ji et al., 1997). Experimental studies, however, reveal that rocks can undergo a limited elastic strain and that too at upper crustal levels only; consequently, the elastic models appear unsuitable for characterizing deformations of rocks that might have undergone large ductile strain at deeper crustal levels. Application of the theories of hydrodynamics, on the other hand, is more appropriate for modeling deformation behavior of rock systems containing stiff inclusions in a viscous matrix. Using Lamb's (1932) theory of spherical harmonics, Gay (1968) has modeled the deformation of floating inclusions within a matrix with respect to the bulk strain, for different viscosity contrasts between the inclusion and the matrix. He derived the velocity functions as follows:

Velocity components outside the inclusion:

$$u' = \frac{1}{2}A_{-3}\rho^3 x\left(x^2-y^2\right)/r^5 + B_{-3}\rho^5\left[-5x\left(x^2-y^2\right)/r^7 + 2x/r^5\right] + \dot{\bar{\varepsilon}}x$$

$$v' = \frac{1}{2}A_{-3}\rho^3 y\left(x^2-y^2\right)/r^5 + B_{-3}\rho^5\left[-5y\left(x^2-y^2\right)/r^7 - 2y/r^5\right] - \dot{\bar{\varepsilon}}y \quad (1)$$

Velocity components inside the inclusion:

$$u = A_2\rho^{-2}\left[(5/21)xr^2 - (2/21)x(x^2-y^2)\right] + 2B_2x$$

$$v = A_2\rho^{-2}\left[-(5/21)yr^2 - (2/21)y(x^2-y^2)\right] - 2B_2y \quad (2)$$

where $r=\sqrt{x^2+y^2}$; $\rho = b/\sqrt{1-e^2\cos^2\alpha}$, e is the eccentricity of the elliptical inclusion $(\sqrt{a^2-b^2})$, a and b are the major and minor axial dimensions of the inclusion, respectively; A, B are constants, which need to be determined by applying boundary conditions. $\dot{\bar{\varepsilon}}$ is the principal rate of natural strain in the far field.

Gay's work revealed that the deformation within the inclusion (Eq. (2)) is essentially homogeneous, whereas the deformation outside the inclusion (Eq. (1)) is heterogeneous, as also obtained from elastic models (Eshelby, 1957, 1959). However, in Gay's mathematical formulation it is not explicit how rotating inclusions induce heterogeneity in the matrix flow, although from Lamb's theory one can also determine the velocity functions around a spherical rigid body in terms of its rotation rate by solving the famous Navier–Stoke's equation (Oertel, 1965). This has been utilized to model different aspects of heterogeneous deformation around rigid inclusions, such as particle paths, strain distribution, distortion patterns of foliations (Masuda and Ando, 1988), porphyroclast tails (Bjornerud and Zhang, 1995) and inclusion trail patterns within synkinematic porphyroblasts (Masuda and Mochizuki, 1989) assuming a Newtonian rheology for the matrix.

Masuda and Ando (1988) have expressed the velocity functions outside a rigid, spherical inclusion as:

$$(u_a, v_a, w_a) = (u_{a1}, v_{a1}, w_{a1}) + (u_{a2}, v_{a2}, w_{a2}) \tag{3}$$

The first part of the right hand side of the equation refers to the velocity components considering a general viscous flow around a fixed rigid spherical body, whereas the second part represents the velocity components arising due to the rotational motion of the rigid body. The expressions of these velocity components are as follows:

$$u_{a1} = \sum_{n=1}^{\infty} \left\{ \frac{(n+1)r^{1-2n}}{n(2n+1)(2n-1)} \frac{\partial}{\partial x}\left(r^{2n+1}\chi_{-n-1}\right) - \frac{r^2}{2(2n+1)} \frac{\partial}{\partial x}\chi_{-n-1} + \frac{\partial}{\partial x}\phi_{-n-1} + \left(z\frac{\partial}{\partial y} - y\frac{\partial}{\partial z}\right)\psi_{-n-1} \right\} \tag{4}$$

where $r = \sqrt{x^2 + y^2 + z^2}$ and χ_n, ϕ_n and ψ_n are spherical solid harmonics of degree n.

The form of the expressions of v_{a1} and w_{a1} of Eq. (3) will be similar as in Eq. (4). The expression of the velocity component in the second part (Eq. (3)) is:

$$u_{a2} = \sum_{n=1}^{\infty} \left\{ \frac{nr^{2n+3}}{(n+1)(2n+1)(2n+3)} \frac{\partial}{\partial x}\left(\frac{\chi_n}{r^{2n+1}}\right) - \frac{r^2}{2(2n+1)} \frac{\partial}{\partial x}\chi_n + \frac{\partial}{\partial x}\phi_n + \left(z\frac{\partial}{\partial y} - y\frac{\partial}{\partial z}\right)\psi_n \right\} \tag{5}$$

The form of the expressions of the other two components will be similar as above.

Similarly, Bjornerud and Zhang (1995) have defined the velocity field by adding two velocity components, one associated with displacement (u_a, v_a, w_a) of material points around the rigid inclusion and the other (u_b, v_b, w_b) with shear-induced rotation of the inclusion. The expressions of these two types of velocity components have been obtained as:

$$u_a = (3Ua/4r^3)(1 - a^2/r^2)x^2 + U(1 - 3a/4r - a^3/4r^3)$$

$$v_a = (3Ua/4r^3)(1 - a^2/r^2)xy$$

$$w_a = (3Ua/4r^3)(1 - a^2/r^2)xz \tag{6}$$

and

$$\text{for } r > a: \; u_b = k\omega_o y a^3/r^3,$$

$$v_b = -k\omega_o x a^3/r^3, \; w_b = 0$$

$$\text{for } r < a: u_b = k\omega_o y, \; v_b = -k\omega_o x, \; w_b = 0 \tag{7}$$

where a is the inclusion's radius, r is the radial distance of the point from the inclusion centre, U is the rate of displacement in the shear direction far

away from the inclusion (Eq. (6)) and ω_o is the rotation rate of the inclusion. The parameter k in Eq. (7) is an index of coupling between the inclusion and matrix, the value of which lie in the range of 0 to 1. $k=1$ implies a non-slip condition at the inclusion/matrix interface.

Masuda and Mizuno (1996a) and Pennacchioni et al. (2000) have further extended the analysis for rigid inclusions hosted in a non-Newtonian matrix. Bjornerud (1989) formulated the heterogeneous strain field surrounding an equant rigid inclusion following the equations of Turcotte and Schubert (1982) and numerically modeled the development of passive folds in the neighborhood of the inclusion similar to the foliation drags obtained by Masuda and Ando (1988). The equations obtained by Bjornerud (1989) are as follows:

$$u_r = U\left\{-1 - a^3/(2r^3) + 3a/2r\right\}\cos\theta$$

$$u_\theta = U\left\{-1 - a^3/(4r^3) + 3a/4r\right\}\sin\theta$$

$$(\text{for } r > a) \qquad (8)$$

where a is the radius of the inclusion; r and θ are polar co-ordinates centred on the sphere; u_r and u_θ are radial and tangential velocity components, respectively and U is the far-field unidirectional flow velocity in the $\theta=0$ direction. It may be noted that Eq. (8) is applicable to fluid flow around a rigid sphere subject to the following conditions. (1) The fluid approaches a uniform velocity far away from the sphere and (2) the rigid sphere is stationary and non-rotating. Thus the velocity functions have to be modified in order to utilize them for describing the flow field around a rigid body under shear deformation.

Recently, some workers (Jezek et al., 1999; Mandal et al., 2000b, 2001a) have utilized Jeffery's (1922) theory to model the heterogeneous flow field and development of related geological structures in a rock system containing rigid inclusions of either equant or inequant shape, under pure shear, simple shear or general type of bulk deformation. This theory is given in three dimensions, describing the velocity field around a rotating ellipsoidal inclusion. The velocity functions of Jeffery (1922) involve a number of complex parameters, the solutions of which can be obtained with the help of numerical methods (Jezek et al., 1999). These parameters can, however, be derived analytically when the Jeffery's theory is considered in two dimensions for circular or elliptical inclusions (Mandal et al., 2001b). In two dimensions the velocity functions of the flow around an elliptical inclusion are somewhat simpler, and their expressions follow:

$$\begin{aligned} u' &= S'_{11}\left[1 - 2A(\alpha+\beta) + F\gamma\right]x' + \frac{1}{2}(S'_{12} + S'_{21}) \\ &\quad \times [2(\alpha D - \beta C) + E\gamma]y' + S'_{12}\,y' \\ &\quad - \frac{2\Delta x' y'}{b'^2 x'^2 + a'^2 y'^2}\left[\frac{1}{2}(S'_{12} + S'_{21}) \right. \\ &\quad \times \left\{\frac{E + 2a'^2 C + 2b'^2 D}{a'^2}\right\}x' \\ &\quad \left. + S'_{11}\left\{\frac{F - 2a'^2 A + 2b'^2 B}{b'^2}\right\}y'\right] \text{ and} \end{aligned}$$

$$\begin{aligned} v' &= S'_{22}\,[1 - 2B(\alpha+\beta) - F\gamma]\,y' \\ &\quad - \frac{1}{2}(S'_{12} + S'_{21})[2(\alpha D - \beta C) - E\gamma]x' \\ &\quad + S'_{21}x' \; - \frac{2\Delta x'\,y'}{b'^2 x'^2 + a'^2 y'^2} \\ &\quad \times \left[\frac{1}{2}(S'_{12} + S'_{21})\left\{\frac{E + 2a'^2 C + 2b'^2 D}{b'^2}\right\}y' \right. \\ &\quad \left. + S'_{22}\left\{\frac{F - 2a'^2 A + 2b'^2)B}{a'^2}\right\}x'\right] \qquad (9) \end{aligned}$$

where $a' = \sqrt{a^2 + \lambda}$, $b' = \sqrt{b^2 + \lambda}$ and $\Delta = a'\,b'$, where a and b are the major and minor semi-axes of the elliptical inclusion, and λ is the elliptical co-ordinates of a point under consideration. S'_{ij} is the instantaneous bulk velocity gradient tensor with respect to axial directions of the inclusion. α, β and γ are geometric parameters, whose expressions in two-dimensions can be written as:

$$\alpha = \int_\lambda^\infty \frac{d\lambda}{a'^2\Delta}, \qquad \beta = \int_\lambda^\infty \frac{d\lambda}{b'^2\Delta},$$

$$\gamma = \int_\lambda^\infty \frac{d\lambda}{a'^2 b'^2 \Delta}$$

The solutions of the above integrals are:

$$\alpha = \frac{2}{(a^2 - b^2)}\left[\frac{a' - b'}{a'}\right],$$

$$\beta = \frac{2}{(a^2 - b^2)}\left[\frac{a' - b'}{b'}\right],$$

$$\gamma = \frac{2}{(a^2 - b^2)^2}\left[\frac{(a' - b')^2}{a'\,b'}\right]$$

The expressions of constants, A, B,... in Eq. (9) (Mandal et al., 2000b, 2001a) are:

$$A = \frac{(a+b)^2}{8}, \qquad B = -\frac{(a+b)^2}{8},$$

$$C = D = \frac{ab(a+b)^2}{4(a^2+b^2)}, \qquad E = -ab\frac{(a+b)^2}{2}.$$

At an instant, points lying outside the inclusion ($\lambda > 0$) will move according to the velocity components shown above, while points either on the surface or inside the inclusion ($\lambda < 0$) will move with velocity components:

$$u = -\omega y \text{ and } v = \omega x,$$

ω is the instantaneous rotation rate of the inclusion, which is given by:

$$\omega = -\frac{a^2(\mathrm{Sin}^2\varphi + S_r\mathrm{Sin}2\varphi) + b^2(\mathrm{Cos}^2\varphi - S_r\mathrm{Sin}2\varphi)}{a^2 + b^2}\dot{\gamma}_b \tag{10}$$

where S_r is the ratio of bulk pure shear and simple shear rates. Eq. (10) reveals that inclusions of equant shape ($a = b$) rotate with a constant angular velocity of $\frac{\dot{\gamma}_b}{2}$ in simple shear as well as in a combination of simple shear and pure shear.

The different theoretical models discussed above can be utilised to run numerical experiments to study the flow pattern and related structures around rigid inclusions as outlined in the following sections.

3. Particle paths around rigid inclusions

Two types of paths have been predicted—one with eye-shaped separatrix and the other with bow-tie-shaped separatrix, which have been presumed to develop in Newtonian and non-Newtonian matrix, respectively (Fig. 2; Passchier, 1994). Later studies, however, have shown that the flow with double-bulge-shaped (i.e. eye-shaped) separatrix (Masuda and Mizuno, 1996a) and bow-tie-shaped separatrix (Pennacchioni et al., 2000) may develop in both the rheological varieties. It appears that in addition to matrix rheology there are other factors that could control the geometry of particle paths, such as shape of rigid inclusions ($R = a/b$) and the ratio of pure shear and simple shear rates (S_r) in the bulk deformation as pointed out by Passchier (1994).

For equant inclusions ($R = 1$) in simple shear type of deformation, the particle paths show a typical eye-shaped separatrix (Fig. 3). The separatrix has a finite dimension across its longer direction, but becomes asymptotic along the length (Fig. 3a, see also Masuda and Mizuno, 1996a). The absence of stagnation points (zero velocity) is a characteristic feature of the flow pattern around the inclusion. With introduction of pure

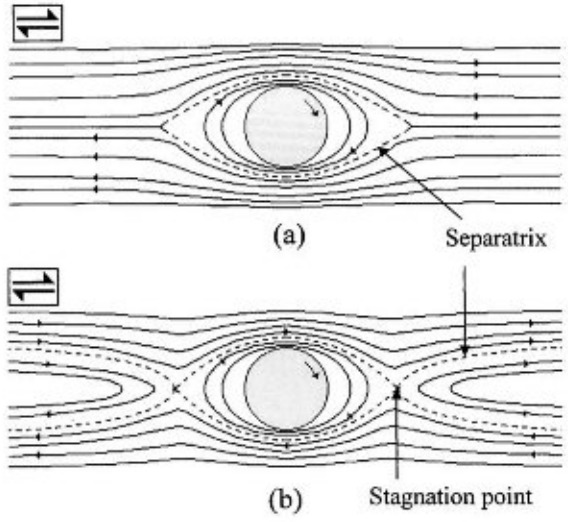

Fig. 2. Possible flow patterns (particle paths) around spherical rigid inclusions under simple shear. (a) Particle paths with eye-shaped separatrix and (b) particle paths with bow-tie-shaped separatrix (Passchier, 1994).

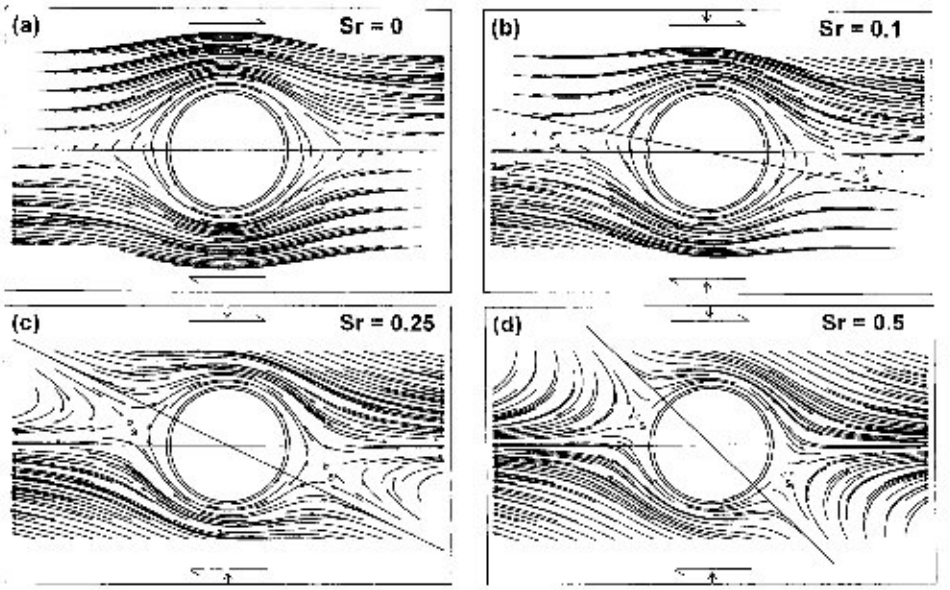

Fig. 3. Numerically simulated particle paths around equant rigid inclusions. (a) Simple shear. (b), (c) and (d) Combination of pure shear and simple shear; straight lines parallel and inclined to the shear direction are the extensional and contractional apophyses of the bulk deformation, respectively. S: stagnation points in the flow around the rigid inclusions. S_r = ratio of pure shear and simple shear rates in the bulk deformation. Note that with increase in S_r, the shape of the separatrix changes from eye shape to bow-tie shape.

shear component in the bulk deformation ($S_r > 0$) the separatrix becomes finite both along and across its length and two diametrically opposite stagnation points appear (Fig. 3b). With further increase in the pure shear component, particle paths in the immediate neighborhood of the inclusion become elliptical and those away from the inclusion are hyperbolic. The separatrix of the two types of paths now assumes a bow-tie-shaped geometry (Fig. 3c). The line joining the stagnation points bisects the extensional and contractional apophyses of bulk deformation (Fig. 3c). The distance between the stagnation points defines the longer dimension of the separatrix. When the pure shear component is very large ($S_r \approx 0.5$), the separatrix shrinks in size and becomes more equant, as the stagnation points moves close to the inclusion (Fig. 3d).

To summarize, the flow pattern around an equant rigid inclusion in simple shear is characterized by a semi-infinite eye-shaped separatrix, which in bulk deformations by a combination of simple shear and

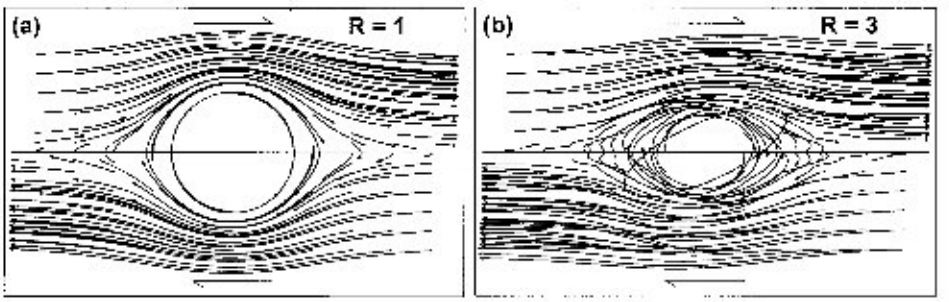

Fig. 4. Diagram showing contrasting flow patterns around (a) equant and (b) inequant rigid inclusions, as obtained from numerical simulation. In (b) the long axis of the inclusion was initially parallel to the shear direction. R: aspect ratio of the inclusion.

pure shear assumes a bow-tie-shaped geometry with finite dimensions (Mandal et al., 2001b).

The flow patterns around inequant inclusions are much more complex, and are characterized by mutually disharmonic, and intersecting particle paths, implying an unsteady nature of the flow (Mandal et al., 2001b, Fig. 4). In contrast to paths around equant inclusions (Fig. 4a), they reverse the movement direction several times while moving along close paths (Fig. 4b). The reversal points are generally located away from the central shear plane.

4. Strain shadow zones around inclusions

In this review we deal mainly with strain shadows developing in the matrix that remain attached to the inclusion. Recent studies (Mandal et al., 2001b) reveal that the development of such strain shadows depends on different geometrical and kinematic parameters, such as shape and orientation of the inclusions, and the ratio of pure and simple shear rates (S_r) in the bulk deformation.

In simple shear type of deformation ($S_r=0$), strain shadow domains develop against the two extensional faces of the equant inclusion describing a σ-type geometry (Fig. 5a). The zones of high strain occur near the contraction face of the inclusion and along long bands at an angle less than 45° with the shear direction (Fig. 5a and b, see also Masuda and Ando, 1988). The low-strain zones tend to shrink as the pure shear component in the bulk deformation increases (Fig. 5b and c), and when the deformation is entirely by pure shear, no strain shadow zone occurs (Fig. 5d).

In case of inequant inclusions the initial axial orientation of the inclusion with respect to the shear

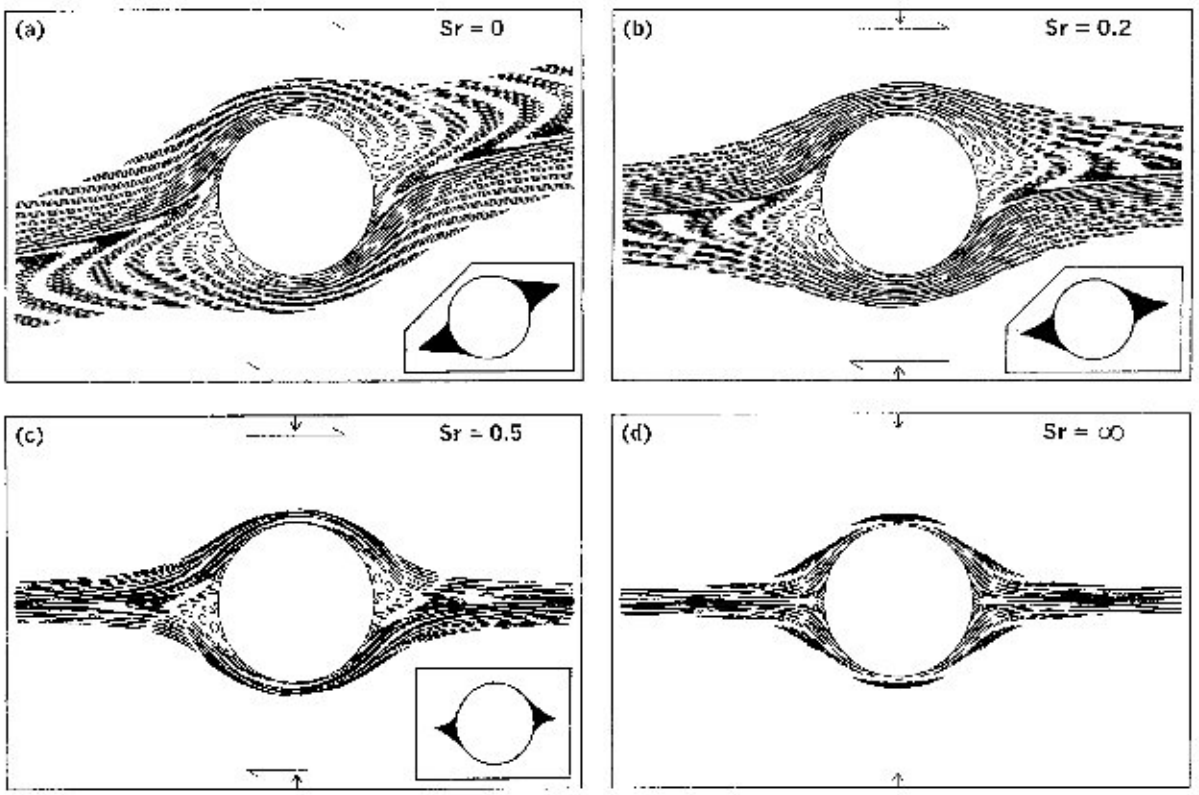

Fig. 5. Strain distributions around equant rigid inclusions in numerical models. Finite bulk shear = 4.0. Strain shadow zones (shaded) are shown in insets.

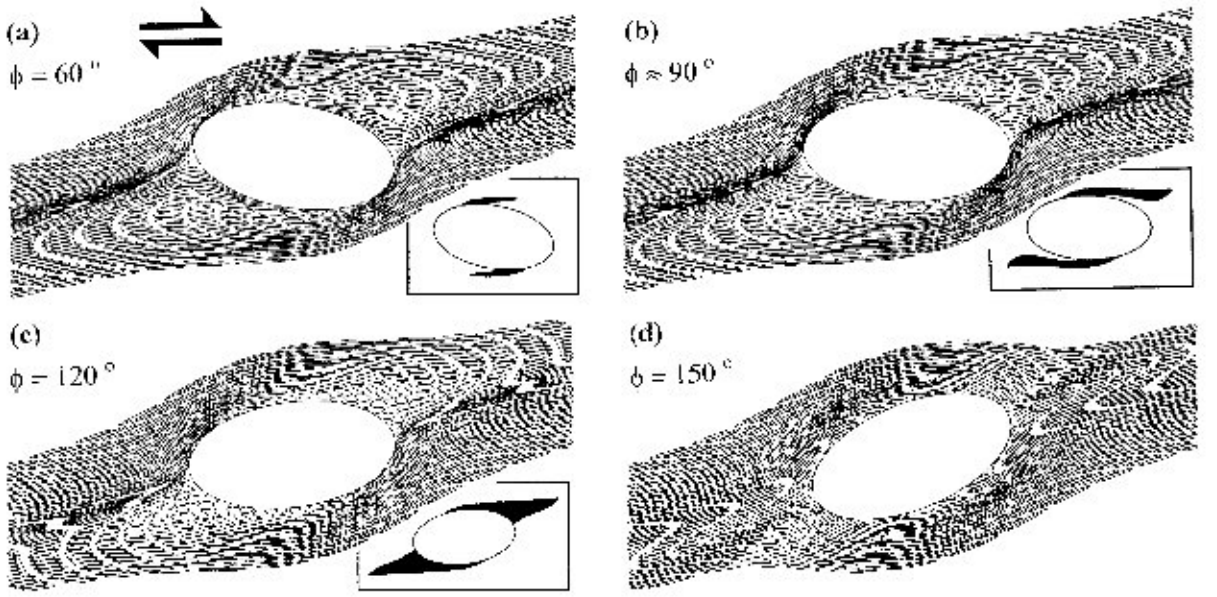

Fig. 6. Strain distributions around inequant inclusions of aspect ratio $R=2$ with different initial inclinations of their long axes to the shear direction (φ). Finite bulk shear=4.0. Strain shadow zones (shaded) are shown in insets.

direction (φ) and the axial ratio of the inclusion (R) are additional parameters in the localization of strain shadow zones. Strain shadow zones form when the long axis of the inclusion makes an angle between 60° and 135° with the shear direction (Fig. 6). When φ is close to 60°, the strain shadow zone forms a narrow tail, emerging from the tip of the inclusion (Fig. 6a). With increase in initial inclination, the shadow zone becomes wider and longer (Fig. 6b), and at $\varphi=120°$, they form bands giving rise to an overall pattern similar to that of augen structures (Fig. 6c). The low-strain zones die out as the initial inclination of the inclusion is further increased (Fig. 6d) and instead a narrow zone of strong strain concentration appears sub-parallel to the long axis of inclusion (Fig. 6d).

For a given φ, with increase in axial ratio of the rigid inclusion strain shadow zones progressively increase in length as well as change their pattern (Fig. 7). When the axial ratio is low ($R=1.5$), the strain shadow zones resemble σ-type tails emerging from the nodes of the inclusion (Fig. 7a). With increase in axial ratio, R, the zone forms wings, which finally becomes like a band surrounding the inclusion (Fig. 7b,c).

5. Distortion patterns of passive foliations

The heterogeneous flow field around rigid inclusions is commonly manifested in the distortion of passive markers (bedding or foliation) in the matrix (Fig. 1b). The distortion patterns of passive markers in the neighbourhood of rigid inclusions are useful in the analysis of progressive deformation as well as kinematic conditions.

Ghosh (1975) and Ghosh and Ramberg (1976) have analyzed different drag patterns by considering the relative rates of rotation of the inclusion and the passive markers in the course of progressive deformation. However, there are distortion patterns that cannot be explained by these analyses. Masuda and Ando (1988) took into account the heterogeneous strain field around equant inclusions and explained diverse types of distortion patterns for different initial orientation of passive markers under simple shear type of bulk deformation. However, the distortion patterns would also depend on the shape and orientation of the inclusion if it is inequant and the ratio of pure shear and simple shear rates in the bulk deformation, as shown in Figs. 8 and 9. The different drag patterns

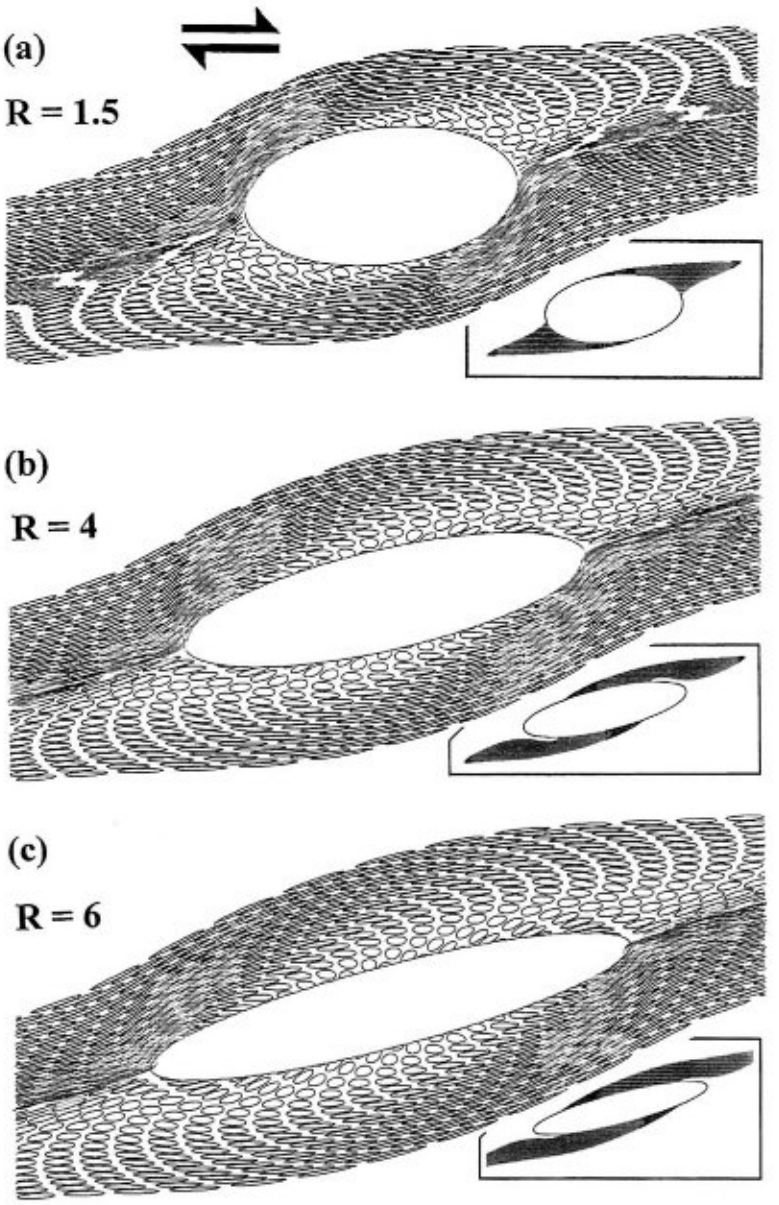

Fig. 7. Geometrical variation of strain shadow zones near inequant inclusions with increase in axial ratio R. The long axis of the inclusions was initially at an angle $\phi = 120^\circ$ with the shear direction.

that may form around rigid inclusions under varying combinations of the above parameters can be classified into four major types (Fig. 10, Mandal et al., 2001b). Type 1: Markers form bi-convex curvatures around the inclusion (Fig. 10a). Type 2: Markers are distorted in the form of typical folds on either side of the inclusion (Fig. 10b). Depending upon the degree of relative curvature, the drag folds can again be classified into three sub types: Type 2a, 2b and 2c. The first two types are characterized by larger curvatures of folds with inward convexity, and they differ from each other by the opposite sense of arrangement

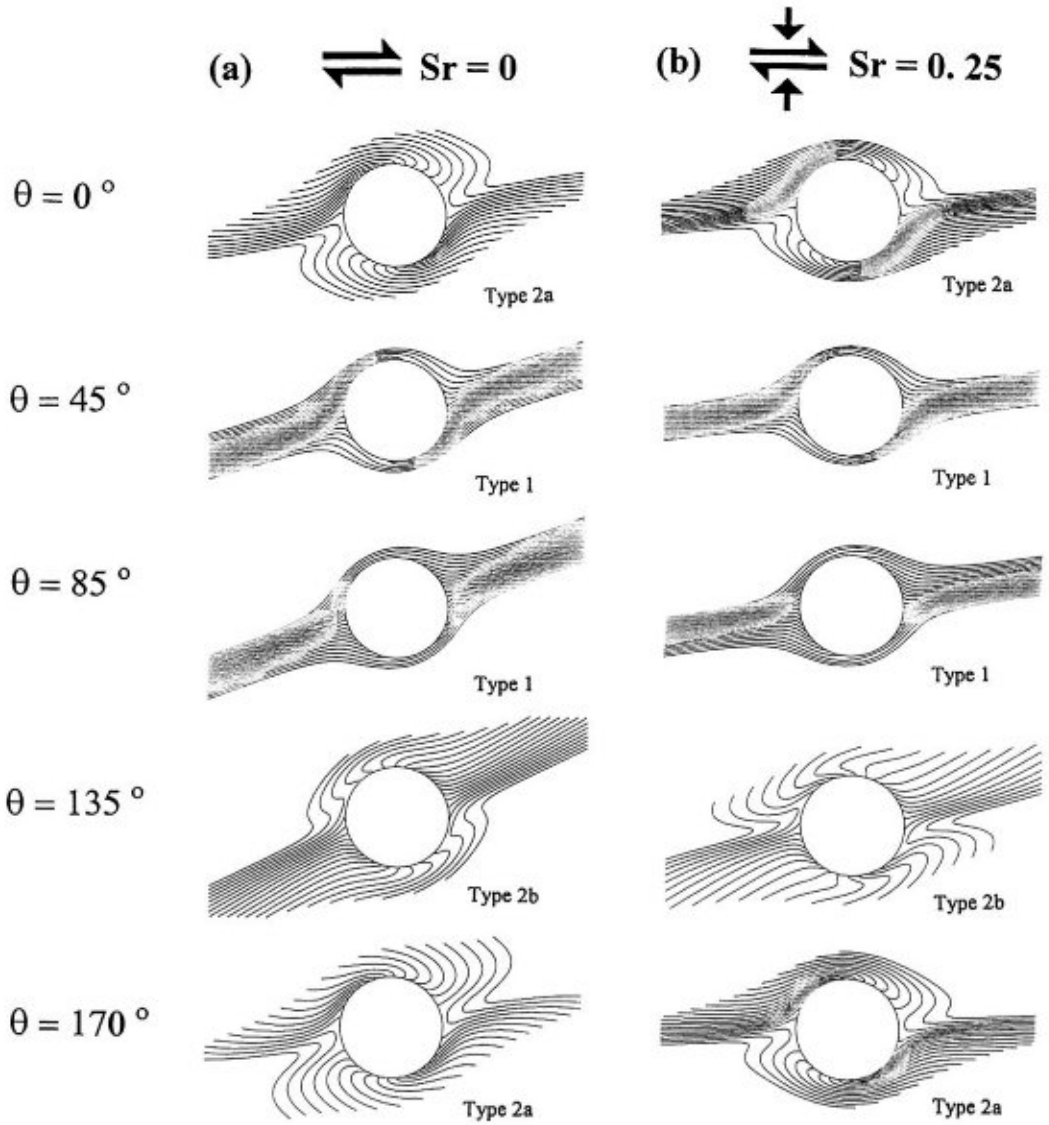

Fig. 8. Numerical simulations of the distortion patterns of passive marker lines around equant rigid inclusions. θ is the initial inclination of marker with the shear direction. (a) Simple shear. (b) Combination of pure shear and simple shear. S_r is the ratio of pure shear and simple shear rates.

of folds with inward and outward curvatures. Type 2c has drag folds with outward convex curvatures much greater than inward convex curvatures. Type 3: Markers are distorted with inward convex curvatures. They have smooth, rounded (single-hinged) (Type 3a) or flat (double-hinged) (Type 3b) crests (cf. millipede structures, Bell and Rubenach, 1986) (Fig. 10c). Type 4: The drag effect of inclusion is such that the markers are distorted in the form of overturned folds on either faces of the inclusion (Fig. 10d). This type of drag patterns has been produced in analog model experiments (Van Der Driessche and Brun, 1987). Types 2c, 3b and 4 develop around inequant inclusions under specific conditions, whereas the rest of the types are

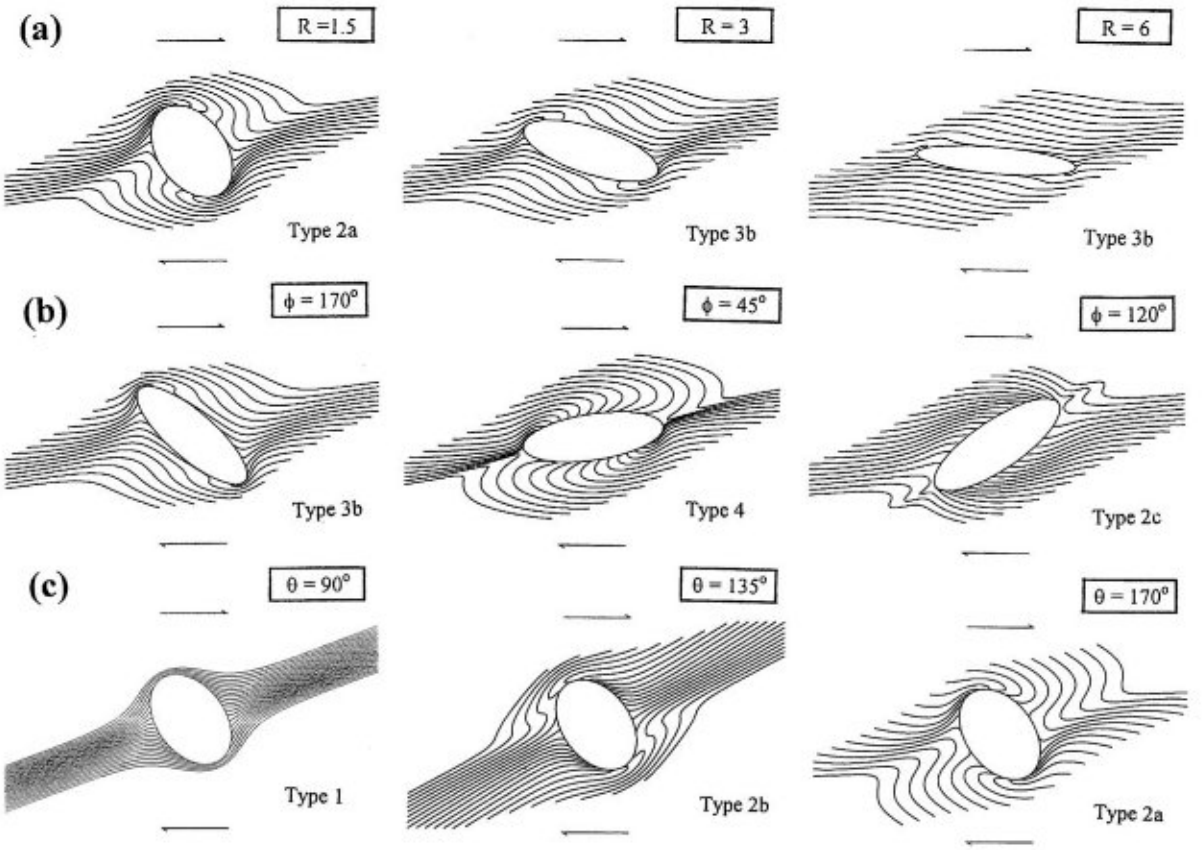

Fig. 9. Drag patterns of marker lines around inequant inclusions. (a) R was varied, keeping $\theta = 0$ and $\phi = 0$. (b) ϕ was varied, keeping $R = 3$ and $\theta = 0$. (c) θ was varied, keeping $R = 1.5$ and $\phi = 0$. In all the cases $S_s = 0$. R: axial ratio of inclusion; ϕ: initial inclination of the long axis of inclusion with the shear direction; θ: initial inclination of marker with the shear direction.

common to both equant and inequant inclusions. The nature of drag pattern of marker foliation may be useful to understand their initial orientations as well as the shear sense. For example, in case of Type 2 drag patterns the initial orientation of the foliation is required to be parallel to the shear direction or at angles more than 90°. Again, Types 2b and 4 drag patterns can be used as shear sense indicators (Fig. 11). Table 1 summarizes the conditions at which different types of drag patterns develop.

6. Mantle structures around porphyroclasts

Passchier (1994) has comprehensively classified mantled porphyroclasts (Fig. 1c) into four types (θ-, δ-, ϕ- and σ-type, Fig. 12). θ-type porphyroclasts are characterized by little or undeformed mantles without any discernible tails. σ- and δ-type porphyroclasts have mantles with prominent tails showing monoclinic arrangement. The tails on either side of the porphyroclasts lie at relatively different levels, defining *stair-stepping* (Fig. 12). σ-type porphyroclasts have tails bounded by straight lines on one side and curved lines on the other side that define an internal asymmetricity. The tails in σ-type porphyroclasts do not cross the shear plane passing through the center of the porphyroclast. In contrast, δ-type porphyroclasts have tails with both boundaries curved in the same sense, and in addition, the tails cross the central shear plane. ϕ-type porphyroclasts, on the other hand, have tails symmetrically disposed astride the rigid core

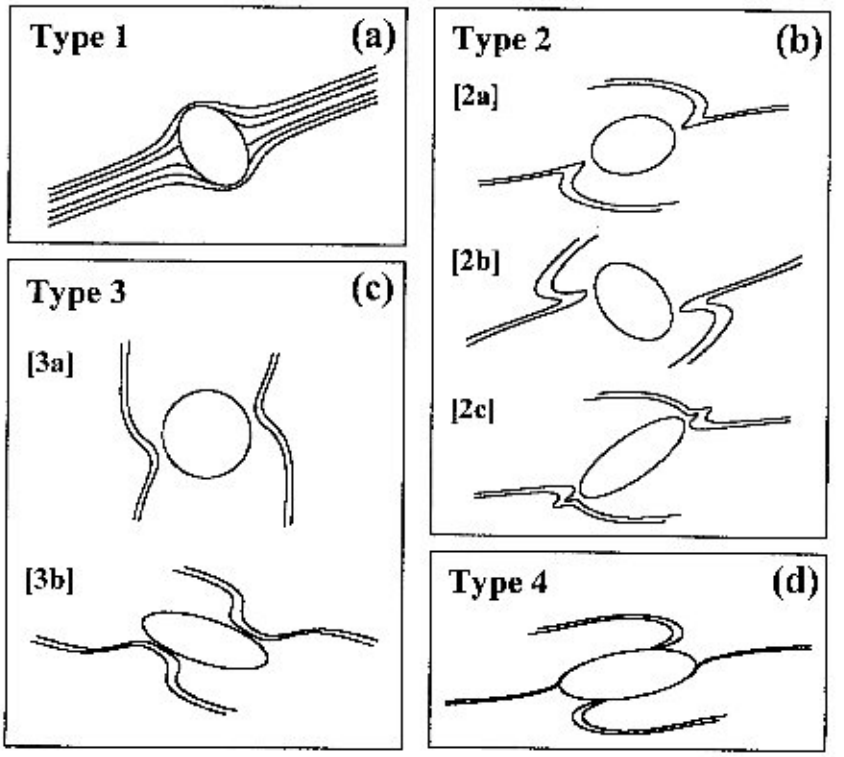

Fig. 10. Types of drag patterns obtained from numerical simulations (see text for details).

showing an orthorhombic symmetry. σ- and δ-type porphyroclasts can be used as shear sense indicators by analyzing the sense of stair-stepping as shown in Fig. 12. We will see later that there may be more complex mantle structures showing combinations of the above types.

The mantle structures of porphyroclasts have been successfully simulated in experiments with Newtonian as well as non-Newtonian matrix (Passchier and Simpson, 1986; ten Brink and Passchier, 1995; Passchier and Sokoutis, 1993). The experimental results apparently conform to the theoretical genetic models, formulated on the basis of the geometry of flow perturbations around rigid porphyroclasts (Passchier, 1994) barring some deviations (Masuda and Mizuno, 1996b).

Numerical simulation (ten Brink et al., 1993; Bjornerud and Zhang, 1995; Masuda and Mizuno, 1996b) is another useful approach to study the evolution of mantled porphyroclasts. These numerical models show the probable modes of development of mantle structure around equant porphyroclasts in a simple shear type of progressive bulk deformation. However, in natural mylonites porphyroclasts are often inequant in shape (Passchier and Simpson, 1986). In addition, the bulk deformation can have a shortening component across the shear zone. In detail, the shape of natural mantled porphyroclasts are thus likely to be more complex and to deviate from those so far predicted by simulations with inclusions of equant shape under simple shear type of progressive deformation (Passchier and Trouw, 1996). Again, the physical model experiments of Passchier and Simpson (1986) explicitly reveal that the rate of size reduction of the porphyroclast is a crucial parameter controlling the geometry of mantle structures. Mandal et al. (2000b) have presented a more generalized theoretical model in two-dimension, and shown probable patterns of mantle structure around inequant porphyroclasts in a Newtonian matrix. Their numerical simulations

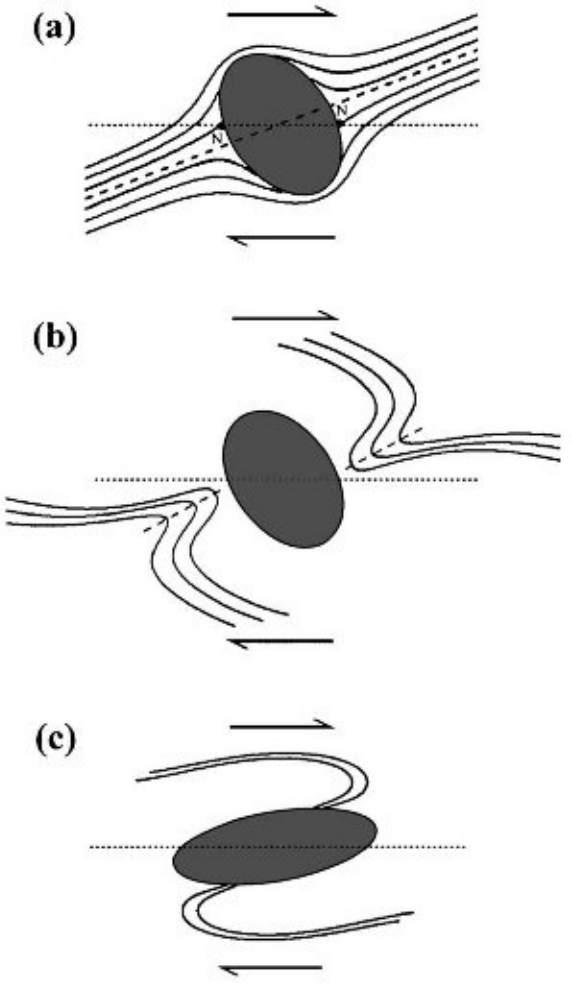

Fig. 11. Drag patterns as shear sense indicators. (a) Side-stepping of null points (N) separating normal and reverse drags. (b) Side-stepping of axial traces (dashed line) of inwardly convex drags. (c) Vergence of overturned drag folds on the long faces of inclusions with a large axial ratio.

attempt to investigate the control of the following factors on the development of tail structures over a large finite strain: (1) the rate of size reduction of porphyroclast; (2) the ratio between pure shear and simple shear rates in the bulk deformation; and (3) the initial shape and orientation of porphyroclasts (represented by the aspect ratio *a*/*b*). This model, when applied for an equant clast and simple shear type of progressive deformation, yields results similar to those of earlier models.

In order to describe porphyroclast mantles, we need to define the following terms. *Porphyroclast mantle* — recrystallized, ductile rim of the porphyroclast. *Mantle structure* — deformed geometry of the mantle around the rigid core of a porphyroclast. *Tails* — the portions of deformed mantle on either side of the rigid core. *Wing* — narrow offshoots of a tail (Fig. 13a). Branch point — the point from which a wing offshoots from the tail. *Wing migration* — the bodily migration of a wing along with the branch point (Fig. 13b). *Wing lengthening* — the increase in length of a wing, which occurs in two modes — (1) shifting of the branch point without wing stretching, (2) wing stretching without branch point shifting (Fig. 13c). *Contractional face and extensional face* — portions of the inclusion, at any instant, facing the contractional and extensional fields, respectively (Fig. 13a). Side-stepping — refers to the lateral offset of the tails on either side of a porphyroclast (Fig. 13d).

Numerical models of Mandal et al. (2000b) indicate that δ-, ϕ- and finally σ-type mantle structures (Passchier, 1994) develop as the rate of clast-size reduction increases (Fig. 14). These results qualita-

Table 1
Fields of different types of drag patterns around inequant rigid objects (R=3) in the $\phi-\theta$ space

Inclination of marker (θ) \ Inclination of long axis of object (ϕ)	0	45	90	135	180
0	Type 3b	Type 4	Type 4	Type 2c	Type 3b
45	Type 1	Type 1	Type 4	Type 1	Type 1
90	Type 1	Type 1	Type 1	Type 1	Type 1
135	Type 2c	Type 2b	Type 3a	Type 3b	Type 2c
180	Type 3b	Type 4	Type 4	Type 2c	Type 3b

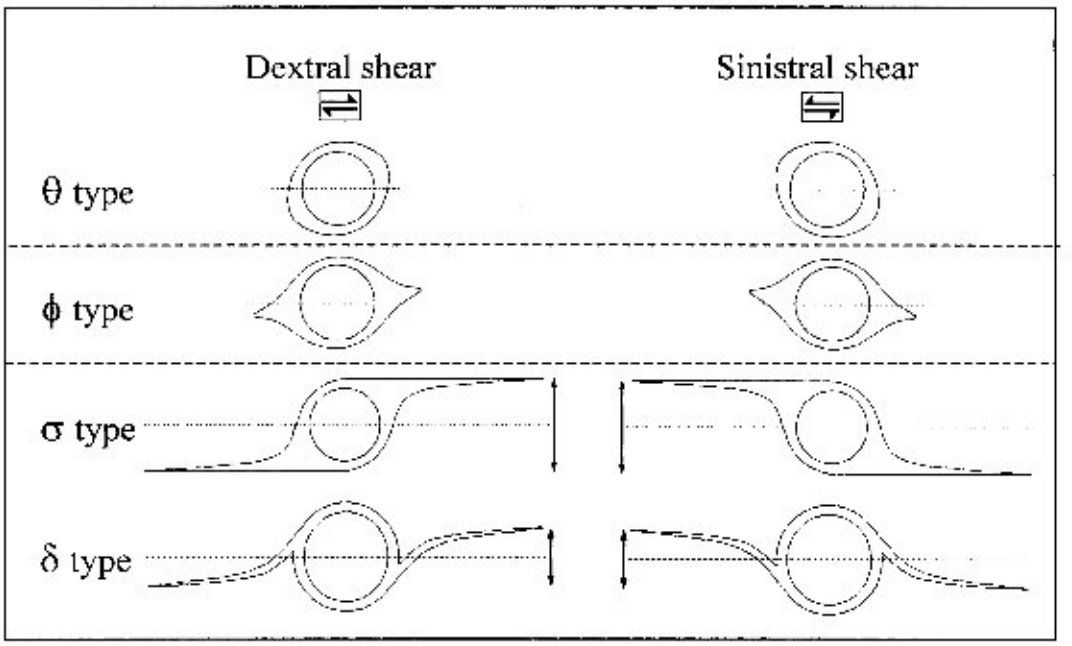

Fig. 12. Types of porphyroclast systems (Passchier, 1994). Relations between the sense of stair-stepping of σ- and δ-type porphyroclast tails and the sense of bulk shear are shown by double headed arrows.

tively conform to the model of Bjornerud and Zhang (1995) that shows the development of σ-type inclusions at a high rate of recrystallization. Similar results were also obtained from analog model experiments (Passchier and Simpson, 1986). For a given rate of clast-size reduction, the mantle geometry changes with increasing finite shear strain during progressive deformation (Fig. 14). The stability fields of the principal mantle types have been delimited in the space of finite strain versus recrystallization rate from physical and numerical model experiments (Passchier and Simpson, 1986; Bjornerud and Zhang, 1995). These studies are, however, restricted to moderate finite strains ($\gamma \leq 10$). The simulations of Mandal et al. (2000b) and Masuda and Mizuno (1996b) show development of complex but definite patterns over larger finite strains as shown in a broader field diagram (Fig. 15).

It has also been revealed that typical δ-type tails that cross the reference plane and show stair-stepping generally develop for moderate rates of clast-size reduction (0.25–0.5). When the rate of clast-size reduction is lower, the mantle structure looks like incipient δ-type tails that do not cross the reference plane, which at lower values of kinematical vorticity number (i.e. higher S_r) appear as δ objects without stair-stepping but showing side-stepping as defined in Fig. 13 (Fig. 16, see also Passchier et al., 1993).

For the same kinematic and physical conditions, porphyroclasts of different initial shapes develop different patterns in their mantles (Fig. 17). At a low finite strain, elongate inclusions with larger aspect ratio have more complex multi-winged tail patterns in comparison to those of equant inclusions, except at higher values of clast-size reduction rate. In natural mylonites the former may be mistaken to represent high finite shear. Such a qualitative assessment of finite strain from mantle structures may thus be erroneous unless other factors are taken into account. At higher values of S_r inequant inclusions also show development of δ-like tails that do not cross the central reference plane and appear as non-stair stepped δ-tails of Passchier et al. (1993). However, the mantle structure shows side-stepping (Fig. 18).

Mandal et al. (2000b) performed several numerical experiments in order to study the effects of orientation

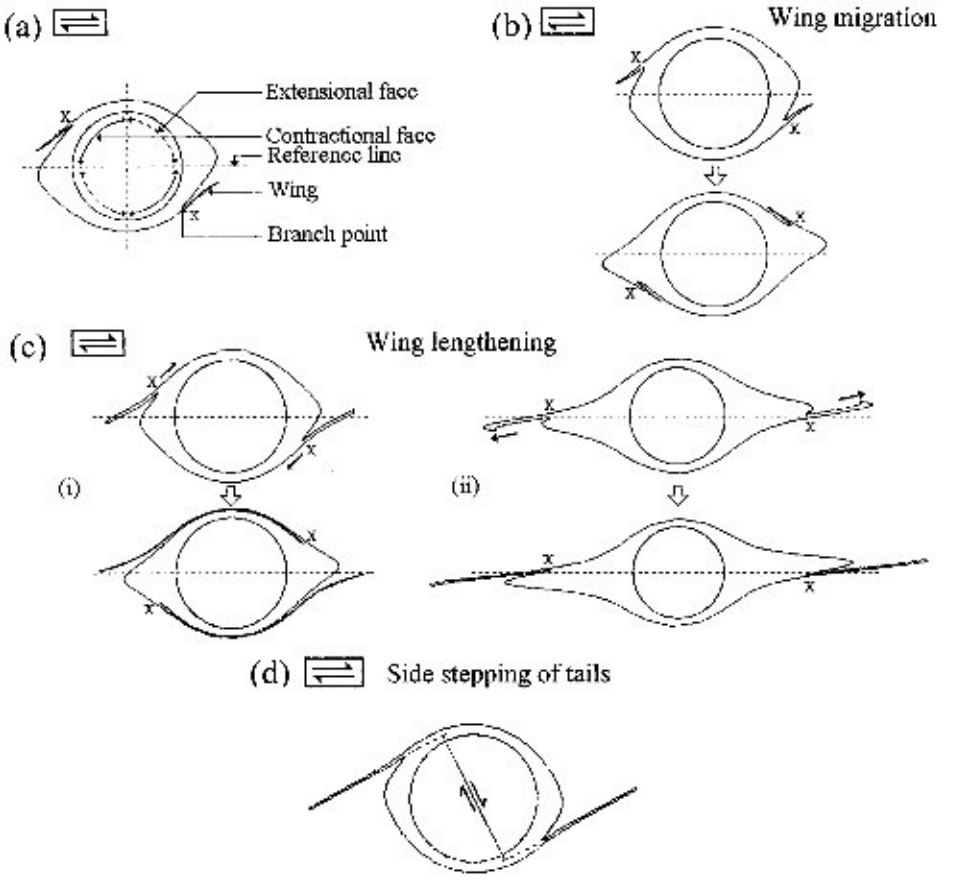

Fig. 13. Diagrammatic representation of the terminology used in the text. (a) Geometrical terms (see text for details); (b) wing migration by shifting of branch points (X); (c) wing lengthening by two modes: (i) shifting of branch points (X) without wing stretching, (ii) stretching of wings without branch point (X) shifting; (d) side-stepping in tail structure.

of inequant porphyroclasts on the mantle geometry. In simple shear type of progressive deformation ($S_r = 0$) porphyroclasts of aspect ratio 1.5 develop σ-type mantle geometry when their long axis is initially parallel to the shear direction (Fig. 19). With increase in the initial inclination ($\varphi > 20°$) the mantle tends to have a composite structure showing δ-type wings, which becomes dominant, giving rise to a δ-type overall geometry of the mantle at $\varphi = 80°$. A similar transformation from σ-type to δ-type mantle geometry with change in porphyroclast orientation has been demonstrated from kinematic models (Simpson and De Paor, 1993). With further increase in the inclination ($\varphi > 110°$) the mantle becomes symmetrical, forming a ϕ-type geometry.

For a given finite bulk shear, the variation of mantle geometry versus initial orientation of porphyroclast, as noticed in the above numerical examples, is different when the porphyroclast has a different initial aspect ratio. Experiments with initial aspect ratio 3 yield a contrasting result (Fig. 20). Porphyroclasts with initial orientation parallel to the shear plane develop δ-type mantle geometry and those with initial orientation perpendicular to the shear plane form σ-type mantle geometry.

Different sets of experiments were run by Mandal et al. (2000b) by varying the initial orientation of porphyroclast under different values of the ratio of pure shear and simple shear rates (S_r) or kinematical vorticity number (W_k) with constant initial aspect ratio

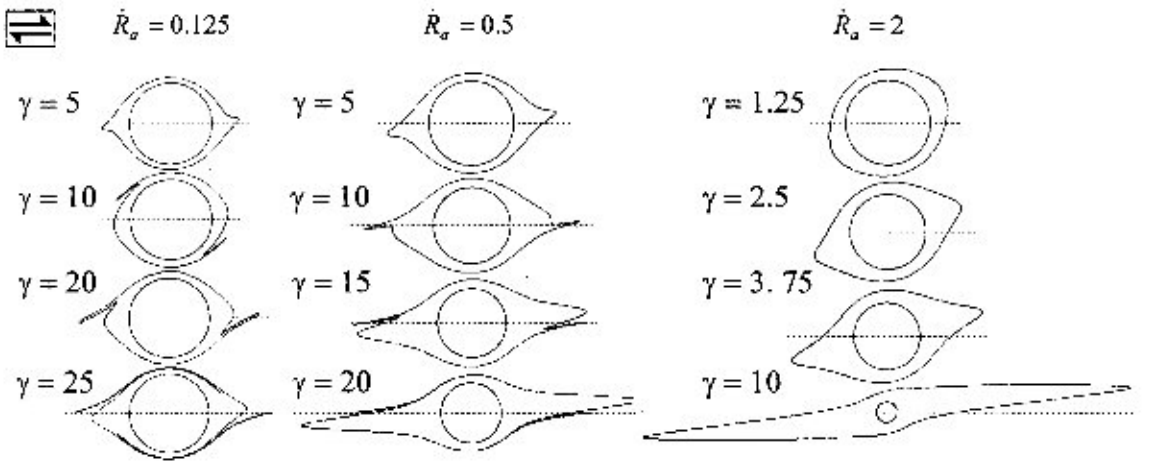

Fig. 14. Numerical simulations of mantle structures around equant porphyroclasts at different size reduction rates. (a) $\dot{R}_a = 0.125$, (b) $\dot{R}_a = 0.5$, (c) $\dot{R}_a = 2$.

($a/b = 2$). The experimental results are shown synoptically in Fig. 21. The mantle pattern, irrespective of initial orientation of porphyroclast, tends to assume a simpler δ-like geometry without stair-stepping at a large value of S_r or a low value of W_k. However, the S_r-value at which porphyroclasts show such a simple pattern depends on the initial orientation (φ) of the porphyroclast. When $\varphi = 0$, the pattern develops at $S_r = 0.50$, which forms at $S_r = 0.25$, when the initial orientation φ is 90°.

6.1. Kinematics of mantle deformation

Numerical experiments, described in the earlier sections, reveal that the development of mantle structures involves some specific kinematics of their tails or wings, which in turn govern the final geometry of the mantle structure. This section presents a genetic basis for different mantled porphyroclast systems by considering the following three modes of mantle deformation. *Mode 1*: The mantle development involves dominantly *wing migration* (Fig. 13); the wings move bodily with the rotating rigid porphyroclast without any shortening or lengthening during migration. *Mode 2*: The mantle development is associated with *wing lengthening* (Fig. 13), that takes place either by branch point *shifting* (Mode 2a) or by wing *stretching* (Fig. 13) without branch point shifting (Mode 2b). *Mode 3*: The tail structures lengthen in the instantaneous extension quadrant along with the branch points.

Each mode of mantle development gives rise to a particular type of mantle structure. In Mode 1 the wings show as incipient δ-like geometry, which bodily migrate and coalesce with ϕ-type tails in the instantaneous extension quadrant, forming a hooked $\delta-\phi$ geometry at a large finite strain (Fig. 15). In Mode 2a, the wings grow in length, but never cross the central reference plane. The mantle therefore does not assume a typical δ-type geometry, as defined by Passchier and Simpson (1986), but forms atypical δ-type structures, which transform into a rolled $\delta-\phi$ composite geometry at a large finite strain (Fig. 15). Mode 2b mantle development is characterized by wing stretching, maintaining the branch points at fixed positions. The wings therefore can cross the central reference line, forming a typical δ-type geometry (Fig. 15). Mode 3 involves stretching of the tail structure as a whole, where the offshoots also experience stretching along with their branch points in the bulk extension direction. This mode of mantle development results in the formation of ϕ-type overall geometry.

Numerical model experiments run at different clast-size reduction rates indicate that the mode of mantle development is controlled by the size reduction rate of the porphyroclast. Low rates of size reduction favour Mode 1 mantle development. As

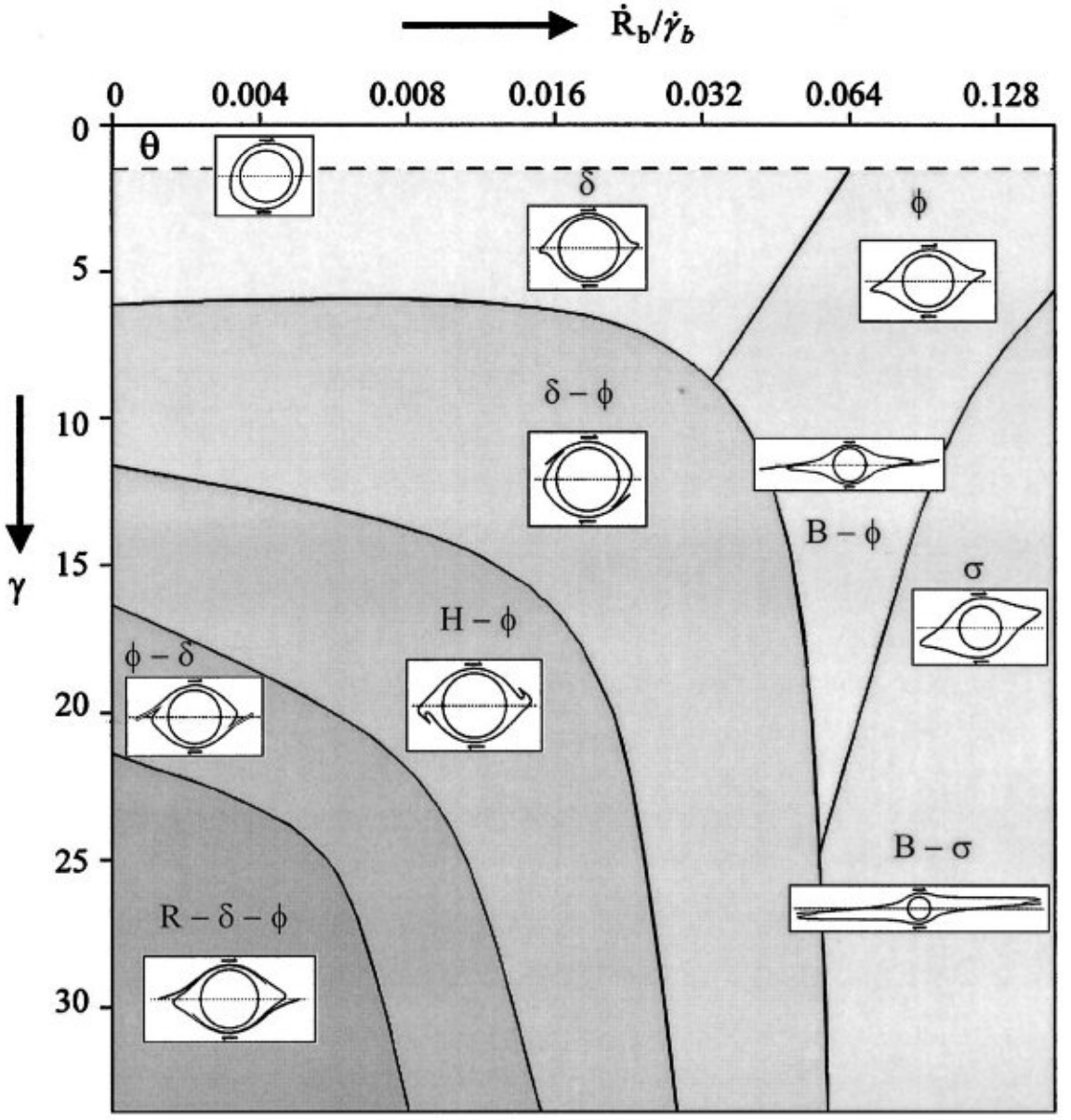

Fig. 15. Fields of different types of mantled porphyroclasts in the space of size-reduction rate (normalized to the bulk shear rate) versus finite bulk shear. $\delta-\phi$: ϕ tail with incipient δ wing; $\phi-\delta$: combination of ϕ- and δ-type geometry; H-ϕ: hooked ϕ; R-$\delta-\phi$: rolled $\delta-\phi$; B-ϕ: branched ϕ; B-σ: branched σ.

the mantle grows in thickness slowly, it experiences a strong drag effect induced by the rotating rigid core. The wings in them therefore migrate bodily, similar to material particles describing close paths around rigid inclusions (Fig. 2). With increase in size-reduction rate, Mode 1 is replaced by Mode 2a. In Mode 2a, the mantle boundary is folded by branch point shifting, forming wings. As the porphyroclast shrinks at a faster rate, the drag influence of the rotating rigid core onto the wings decreases and thereby does not

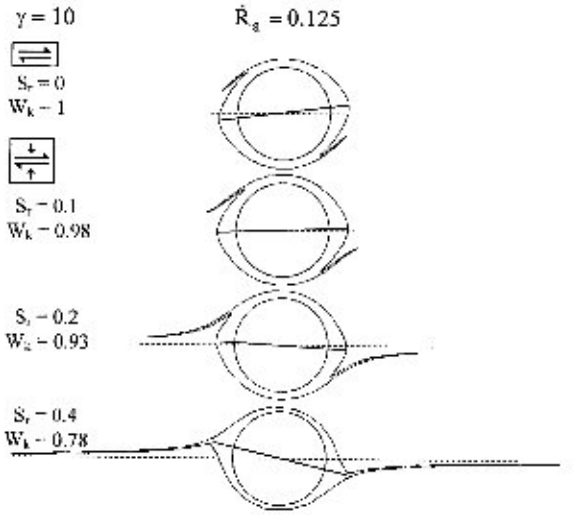

Fig. 16. Influence of the ratio of pure and simple shear rates (S_r) on the pattern of mantle structures around equant porphyroclasts.

result in overall movement of the wing. The wing migration in concert with the rotating rigid core is countered by wing stretching in the bulk extension direction. At a critical balance of these two tendencies the wings do not move bodily either in the shear or extension directions. With further increase in size-reduction rate, the drag of the rigid core onto the mantle boundary becomes weak and the processes of

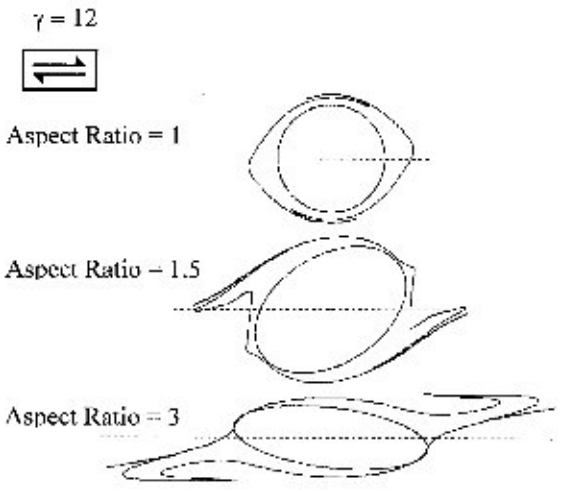

Fig. 17. Control of the shape of porphyroclasts on their mantle structures.

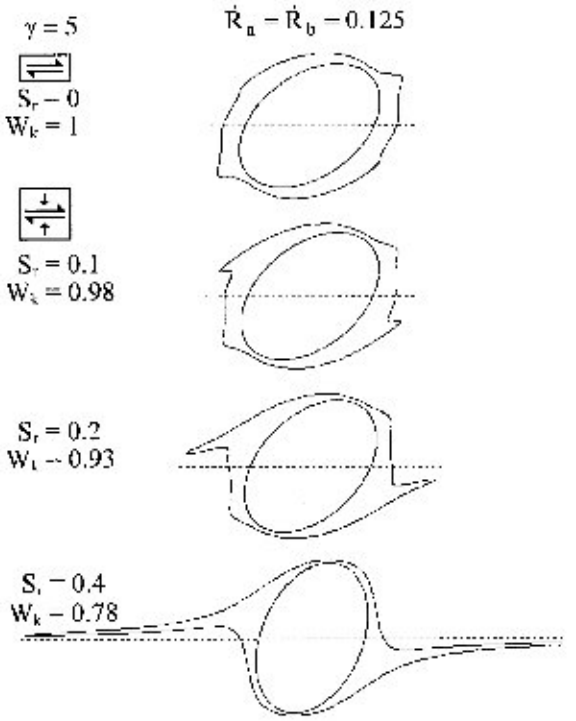

Fig. 18. Control of the ratio of pure shear and simple shear rates on the mantle structures around inequant porphyroclasts of aspect ratio 1.5. Finite bulk shear = 7.5.

branch point shifting due to the drag effect is therefore suppressed, whereas the wing stretching in the extension direction gets dominance. Under this condition Mode 2b becomes the more dominant mode in the mantle development, forming typical δ-type structures. At higher size-reduction rates the mantle grows in size suffering relatively less drag by the rotating porphyroclast. Consequently, Mode 2 is replaced by Mode 3, in which wing stretching is much more important than branch point shifting, giving rise to a ϕ-type overall geometry of the mantle. In Mode 3, σ-type mantle structures form when the drag effect onto the mantle boundary is very little or absent.

7. Inclusion trails within porphyroblasts

Inclusion trails are a typical feature of many natural synkinematic porphyroblasts (Fig. 1d), which commonly record minute details of the deformation his-

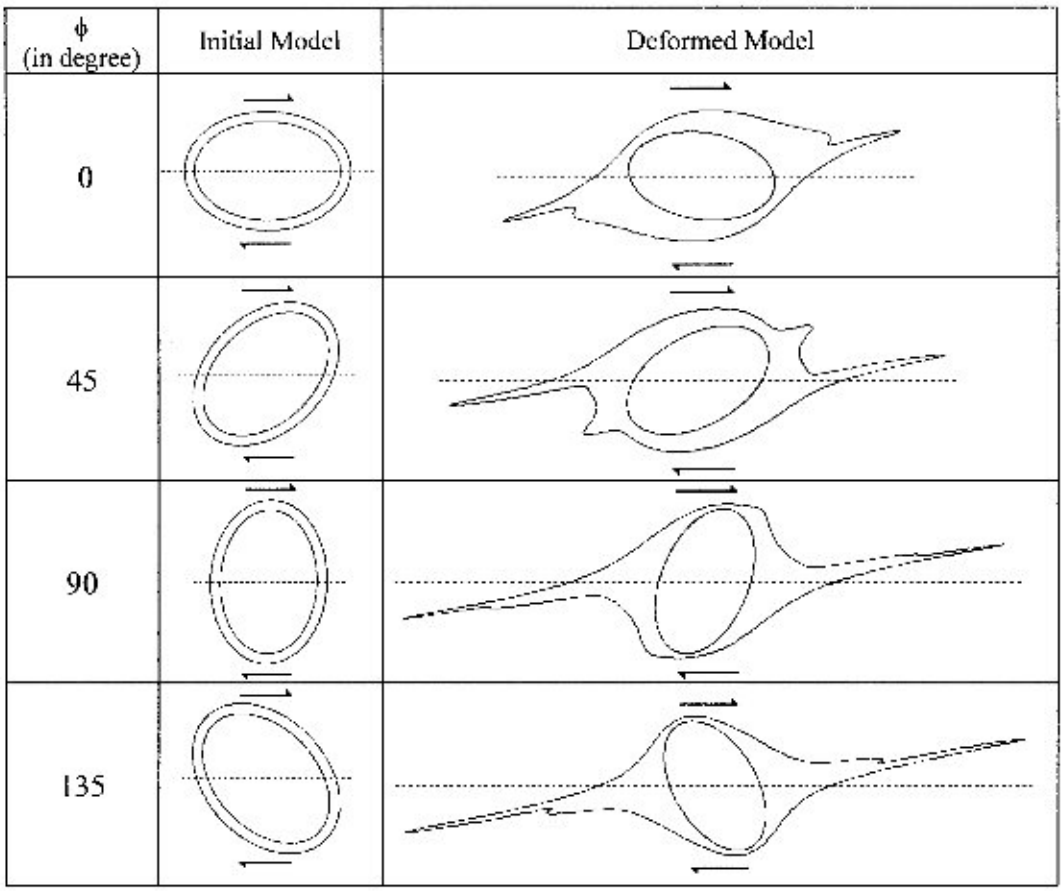

Fig. 19. Variation in the mantle geometry of inequant porphyroclasts (aspect ratio 1.5) with their initial orientation (ϕ). Finite bulk shear = 7.5.

tory. Consequently, the study of porphyroblast systems has been in vogue over several decades (Rast, 1958; Zwart, 1960; Spry, 1969; Rosenfeld, 1970; Schoneveld, 1977; Powell and Vernon, 1979; Bell and Rubenach, 1986; Bell, 1985; Bell and Johnson, 1989; Passchier et al., 1992; Johnson and Bell, 1996; Johnson and Moore, 1996). All the studies on the development of inclusion trails in porphyroblasts are based on two distinctly different models: rotating porphyroblast model and non-rotating porphyroblast model. In the following sections we shall review them separately.

7.1. Development of inclusion trails in rotating porphyroblasts

With the advent of advanced PC software, numerical simulation of trail patterns within rotating porphyroblasts commenced as an area of major interest (Masuda and Mochizuki, 1989; Bjornerud and Zhang, 1994; Beam, 1996). Earlier studies along this line have revealed that relative rates of rotation and growth of porphyroblast are the principal parameters controlling the trail pattern (Mandal and Banerjee, 1987). Beam (1996) has further shown that porphyroblasts can grow by increments of constant radius, constant surface area and constant volume, each producing different trail patterns. Additional complexities in the trail pattern may also arise due to the deflection of foliation in consequence to heterogeneous strain induced by the porphyroblast in its vicinity. Based on the velocity field around a rigid sphere hosted in a viscous matrix with a coherent interface, different patterns of inclusion trails have been simulated numerically by varying the initial orientation of folia-

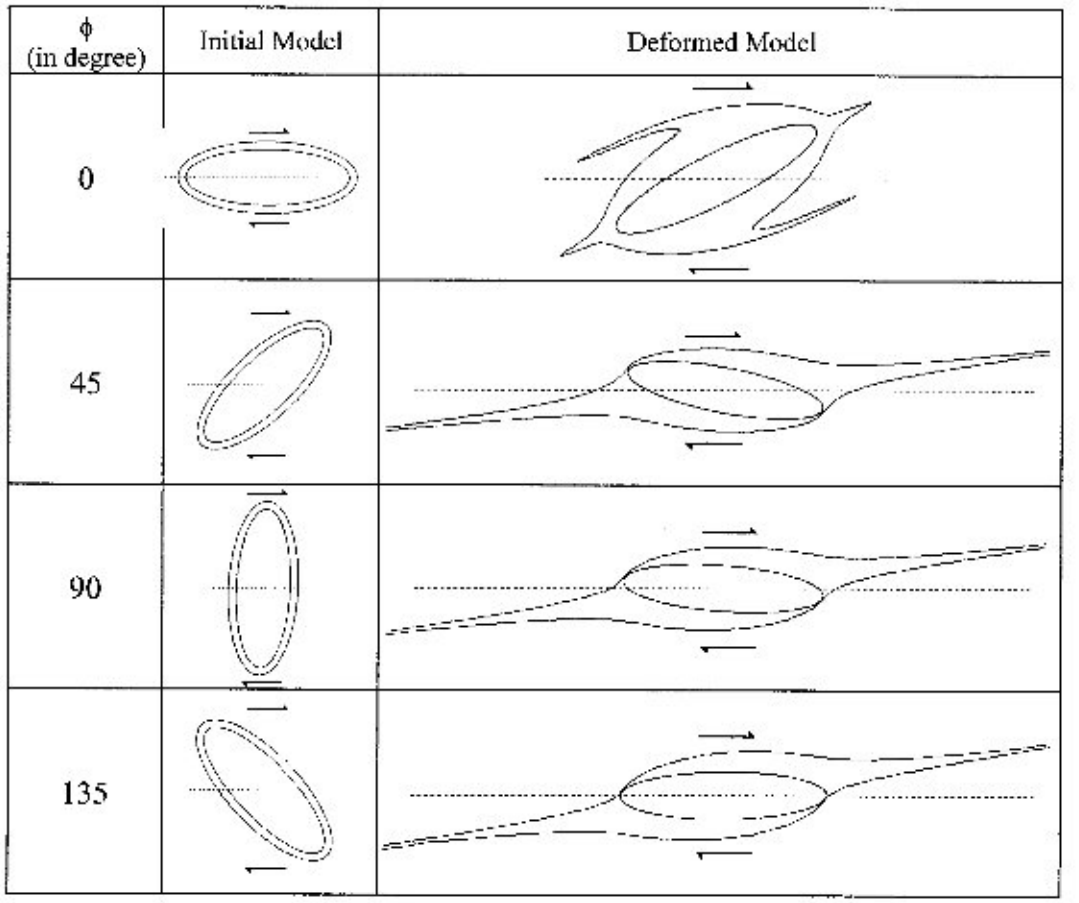

Fig. 20. Variation in the mantle geometry of very elongate porphyroclasts (aspect ratio 3) with their initial orientation (ϕ). Finite bulk shear = 7.5.

tion markers (Masuda and Ando, 1988; Masuda and Mochizuki, 1989). It has been shown analytically that the degree of coupling between the porphyroblast and matrix influences the velocity field, and thereby controls the trail patterns (Bjornerud, 1989; Bjornerud and Zhang, 1994). All these models are two-dimensional and Gray and Busa (1994) advanced them to three dimensions.

The numerical models so far discussed deal with porphyroblasts of equant shape, which rotate with a constant angular velocity. The kinematic analysis reveals that non-spherical porphyroblasts rotate with changing angular velocity during progressive deformation. Beam (1996) has presented a kinematic model for the development of trail structures within non-spherical porphyroblasts under simple shear and a combination of simple shear and pure shear. His model, however, does not consider the effect of heterogeneous strain around the porphyroblast.

Jeffery's velocity functions, given in the earlier section, can be applied to investigate the development of inclusion trails within synkinematic, rotating porphyroblasts of both equant and inequant shapes considering the heterogeneous flow of matrix around the porphyroblast (cf. Jezek et al., 1999; Samanta et al., 2001). The following factors appear to be effective in controlling the geometry of inclusion trails: (1) the initial orientation of foliation markers; (2) the ratio of pure shear and simple shear rates in the bulk deformation; (3) the ratio of the rates of

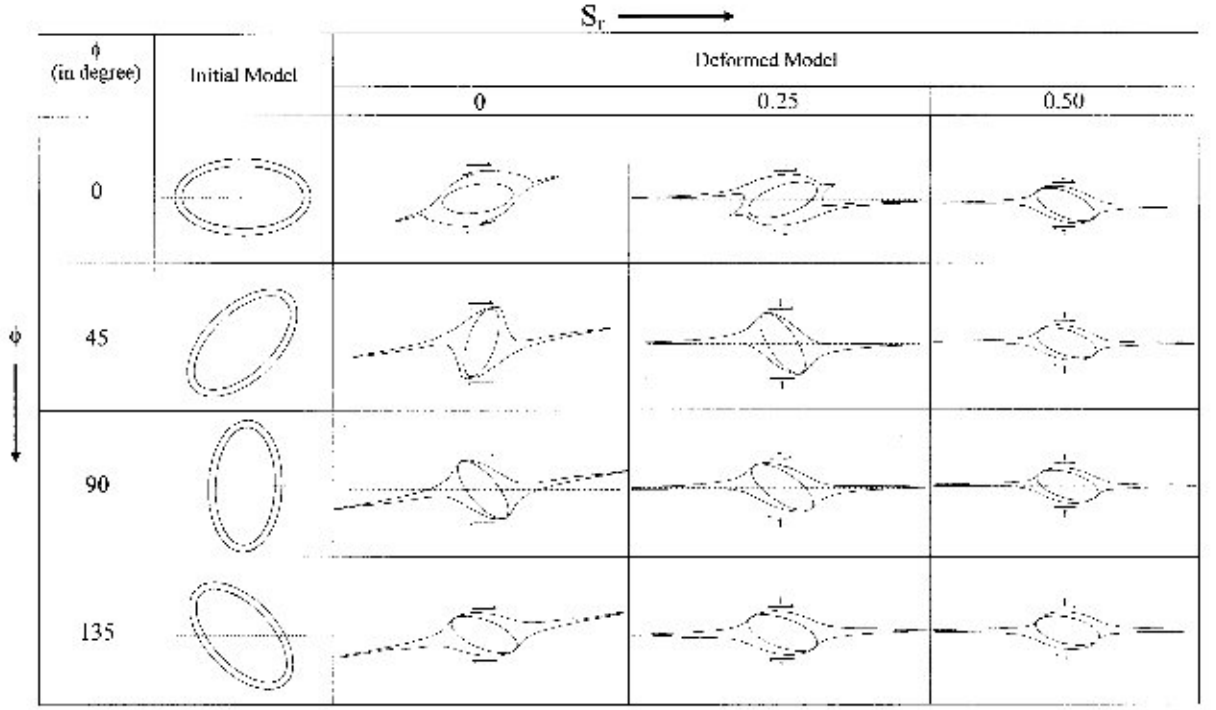

Fig. 21. Distribution of mantle patterns of inequant porphyroclasts ($R = 2$) in ϕ versus S_r space, where φ is the initial inclination of porphyroclast with the shear plane and S_r is the ratio of pure and simple shear rates in the bulk deformation.

rotation and growth of porphyroblast, as illustrated in Figs. 22–25.

In case of inequant porphyroblasts, the initial orientations of the long axis of porphyroblast and the foliation marker, and the ratio of growth rates along the axial directions of porphyroblast are additional factor governing the trail patterns. The diverse trail patterns obtained from these simulations can be classified into a number of types (Fig. 26). Type 1: The central trail is sinuous and confined by outward-convex peripheral trails. Type 2: The trails over the entire porphyroblast are sigmoidal in geometry. Type 3: The central trail is sigmoidal and is confined by inward-convex peripheral trails. Type 3 trails can again be classified into four sub-types. Type 3a: The peripheral trails show a side stepping of their axial traces and the curvature of the trails progressively increases outward. Type 3b: The peripheral trails do not show side-stepping and their curvature progressively decreases outward. Type 3c: The peripheral trails do not show side stepping and their curvature first decreases followed by an increase away from the center similar to those in 'millipede' structure. Type 3d: The central trail is much less curved than the other types and the curvature of the trails progressively increases outward. Type 4: In this pattern peripheral trails are convex outward. The pattern can be further subdivided into two types. Type 4a: the central trail is more or less straight and confined by trails with increasing outward convexity. Type 4b: the central trail has two sinuous segments. Type 5: The peripheral trails are convex inward. Depending upon the pattern of the central trail, the type can again be subdivided into three sub-types. Type 5a: The central trail has two sinuous segments. Type 5b: The central trail with a step-like geometry. Type 5c: a combination of Types 5a and 5b. The kinematic and geometrical conditions for the development of these different types of trail structures are summarized in Table 2.

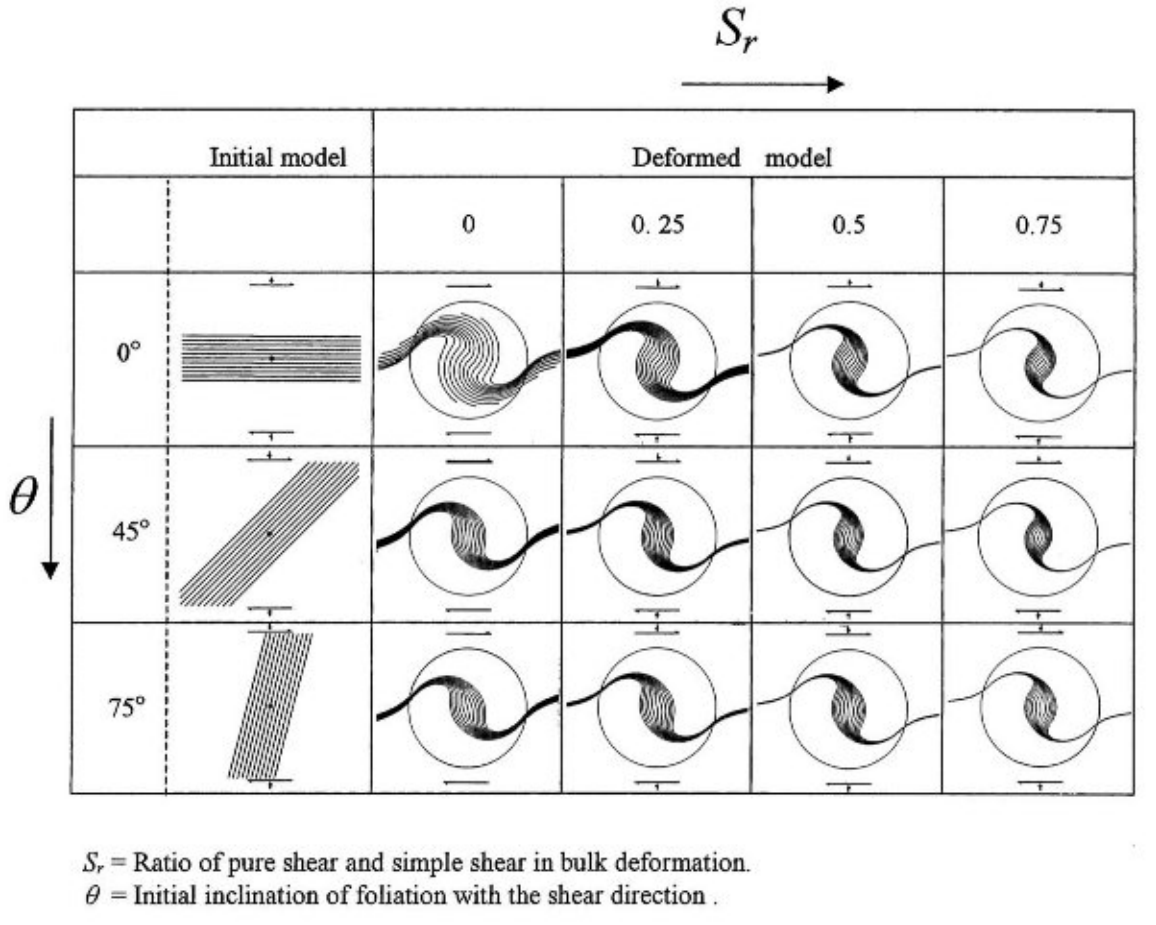

Fig. 22. Inclusion trail patterns in synkinematic porphyroblasts with less than 90°, where θ is the initial orientation of marker. S_r is the ratio of pure shear and simple shear rates. Note that the central trails show reversal in curvatures for large values of S_r. Finite bulk shear in models was 5.

7.2. Development of inclusion trails in non-rotating porphyroblasts

In the models discussed above, the porphyroblast is assumed to rotate with progressive deformation. However, there may be situations where porphyroblasts do not rotate even when the bulk deformation is non-coaxial. For example, Bell (1985) has shown that the rotational component of the bulk deformation is partitioned into zones around the porphyroblasts, and thereby does not induce any rotational motion to the porphyroblast. Similarly, in a heterogeneous system the local rotation of porphyroblasts may be counter balanced by flexural rotation of the unit in which the porphyroblasts occur. As a result, the porphyroblast may overall remain in a stationary state during the bulk deformation (Bell and Hickey, 1997; Stewart, 1997; Hickey and Bell, 1999). In this section we briefly review studies dealing with development of inclusion trails within non-rotating porphyroblasts.

Bell et al. (Bell and Rubenach, 1986; Bell et al., 1997, 1998) have shown that the curved shapes of inclusion trails actually represent parts of crenulation structures over which the porphyroblast grows and preserves the foliations, while those outside of it is entirely overprinted by the later crenulation cleavage (Fig. 27). In multiply deformed terrains porphyroblasts can preserve different generations of crenulation structures in this fashion, giving rise to complex inclusion trail structures (Bell and Johnson, 1989),

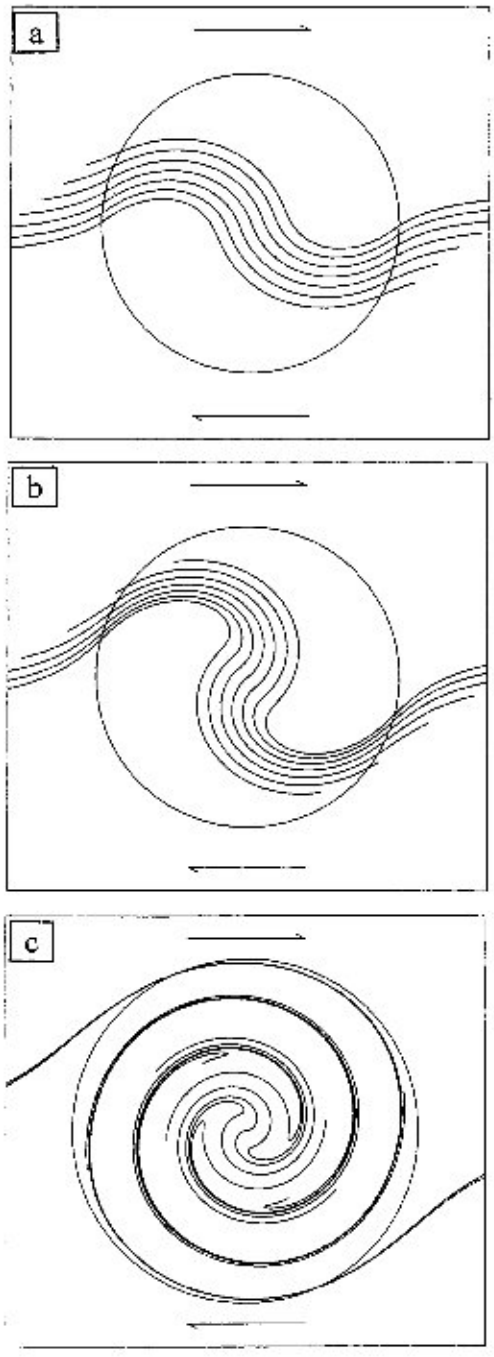

Fig. 23. Sigmoidal to spiral transition of trail patterns with increase in the ratio of rotation and growth rates of porphyroblast. The ratios of rotation rate and growth rate of porphyroblast were 2.5, 5 and 25 Units (1 Unit = 1/length unit) in (a), (b) and (c), respectively. Marker foliation was parallel to the shear direction.

which are often used for unraveling precisely the deformation and metamorphism history of the terrain. In a recent study (Bell et al., 1992), it has been demonstrated that smoothly curving, spiral-shaped inclusion trail structures, which is conventionally believed to be a typical feature of rotated porphyroblasts, can also form in non-rotating porphyroblasts during the overprinting of near-orthogonal foliations in schistose rocks. The smoothening of the foliation with respect to the porphyroblast boundary results from the larger strain localization against faces of porphyroblasts that grow inequantly in the heterogeneous matrix.

It thus appears that the inclusion trail patterns predicted by the models of porphyroblast rotation can also be simulated by these non-rotating porphyroblast models. However, the latter is applicable to systems showing polyphase deformation and metamorphism, where the porphyroblasts grow over multiple events of deformation.

8. Development of fractures in brittle inclusions

Inclusions in rocks often yield in a brittle manner during the deformation, giving rise to diverse types of structures, such as boudins, bookshelf and pull-aparts (Fig. 1e). Such structures are found to be useful kinematic indicators (Mitra, 1978; Hippertt, 1993). However, in order to apply them for structural analyses we need to have a primary idea how a brittle inclusion can undergo failure in response to the flow of the ductile matrix. The concept of fibre-loading theory (e.g. Cox, 1952) is fundamental to the understanding of fracturing mechanics of brittle inclusions hosted in a ductile rock (Ji et al., 1997). Several workers have developed mechanical models for tensile mode of fracturing of inclusions (Hobbs, 1967; Lloyd and Ferguson, 1981; Lloyd et al., 1982; Masuda and Kuriyama, 1988; Ji et al., 1997). However, analog model experiments indicate that besides *tensile fractures* (hereafter called Mode 1), two other modes of fractures occur: *shear fractures* (hereafter called Mode 2a) and *extensional shear fractures* (hereafter called Mode 2b) (Mandal et al., 2001a; Fig. 28). The experimental studies reveal that: (1) brittle inclusions may not rupture until their aspect ratio is larger than a critical value and they attain

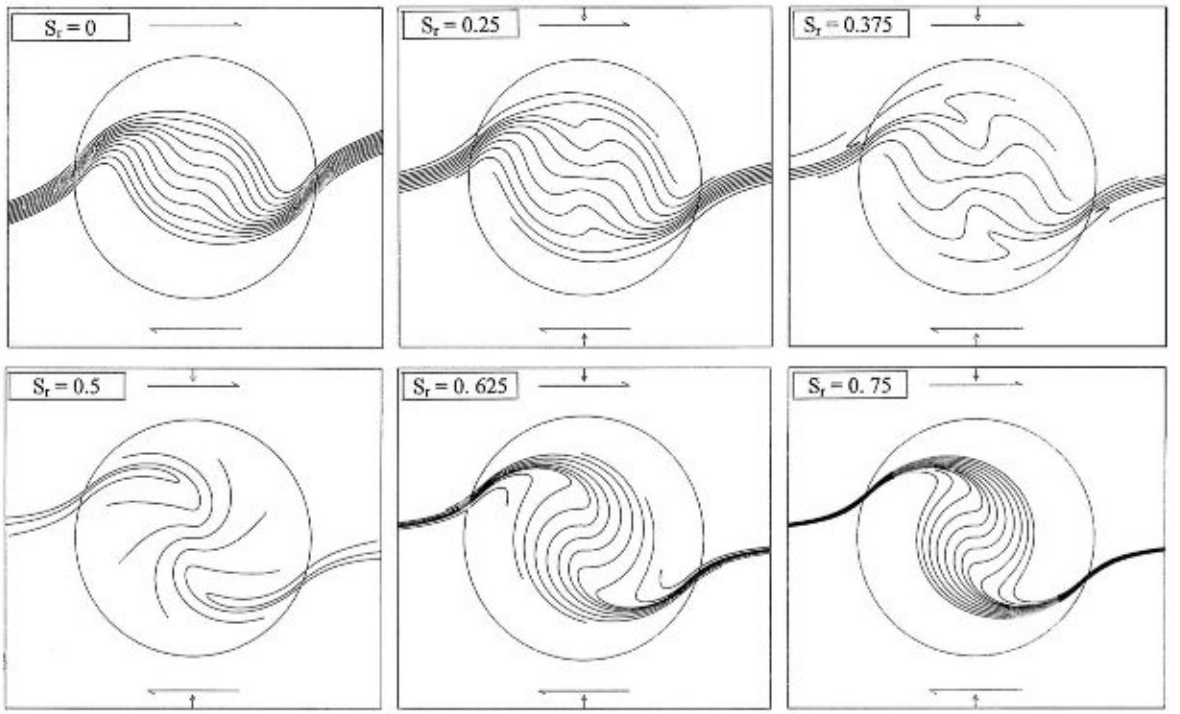

Fig. 24. Inclusion trail patterns in porphyroblasts at different values of the ratio of pure shear and simple shear rates. The foliation was initially at 135° with the shear direction.

orientations with respect to the bulk extension and shear directions within a specific range during deformation; (2) the failure can occur in any of the three modes; (3) the mode of fracturing is sensitive to the aspect ratio and the orientation of the inclusions at the moment of fracturing; and (4) in some situations the tensile fractures may be oblique to the long axis of the inclusion and the bulk extension direction.

8.1. Theoretical formulations

Theoretical modelling of fracture development within brittle inclusions depends fundamentally on how the stress transfer from the ductile matrix to the stiff inclusions is described. Shear-lag models, as applied to geological systems (Ramberg, 1955; Hobbs, 1967; Lloyd et al., 1982; Pollard and Segall, 1987; Masuda and Kuriyama, 1988; Mandal et al., 1994, 2000a; Ji and Saruwatari, 1998) consider traction exerted by the flowing matrix onto the surface of the inclusion and determine the principal tensile stress within the inclusion by balancing the traction on either side of the principal section that lies at right angles to the long axis of the inclusion. When the principal tensile stress on that section exceeds the tensile strength, the inclusion develops tensile fracture along the section. Ramberg (1955) has shown that for rectangular inclusions experiencing axial tension, the maximum principal tensile stress acts on the central section of the inclusion and is oriented normal to its length, producing tensile fractures passing through the inclusion's centre. The expression of maximum axial tension derived by Ramberg (1955) is as follows:

$$\sigma_{xx} = \frac{6\eta\dot{w}_0 a^2}{h^2 H}, \tag{11}$$

where $2a$ and H are the length and thickness of inclusion, h and η are the thickness and viscosity of the embedding viscous layer, $\dot{w}_0$ is the shortening velocity at the boundary of the embedding layer.

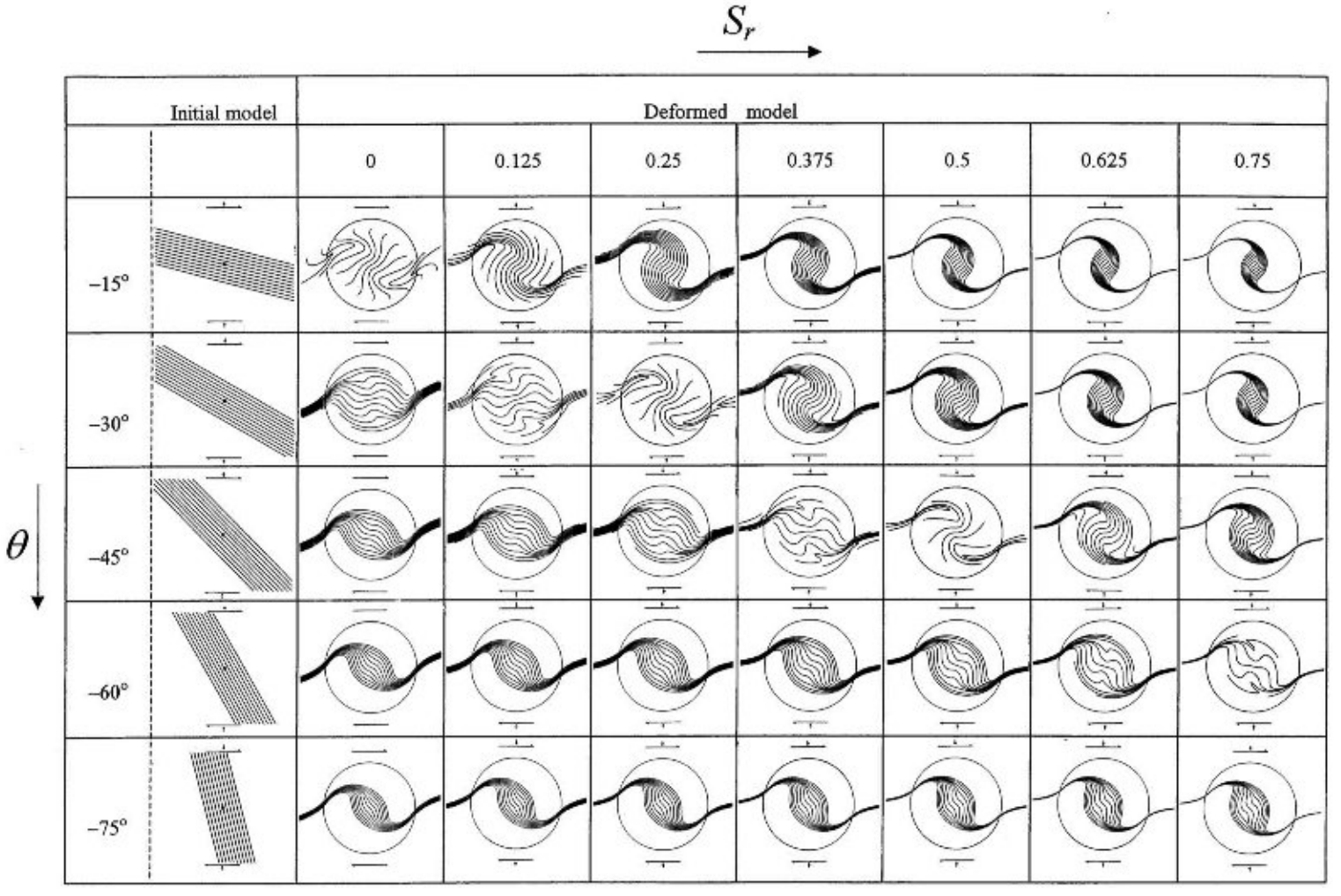

Fig. 25. A map of different trail patterns of porphyroblasts in θ (< 0) versus S_r space. Finite bulk shear in the models was 5. Note development of complex trail patterns at certain combination of S_r and θ values.

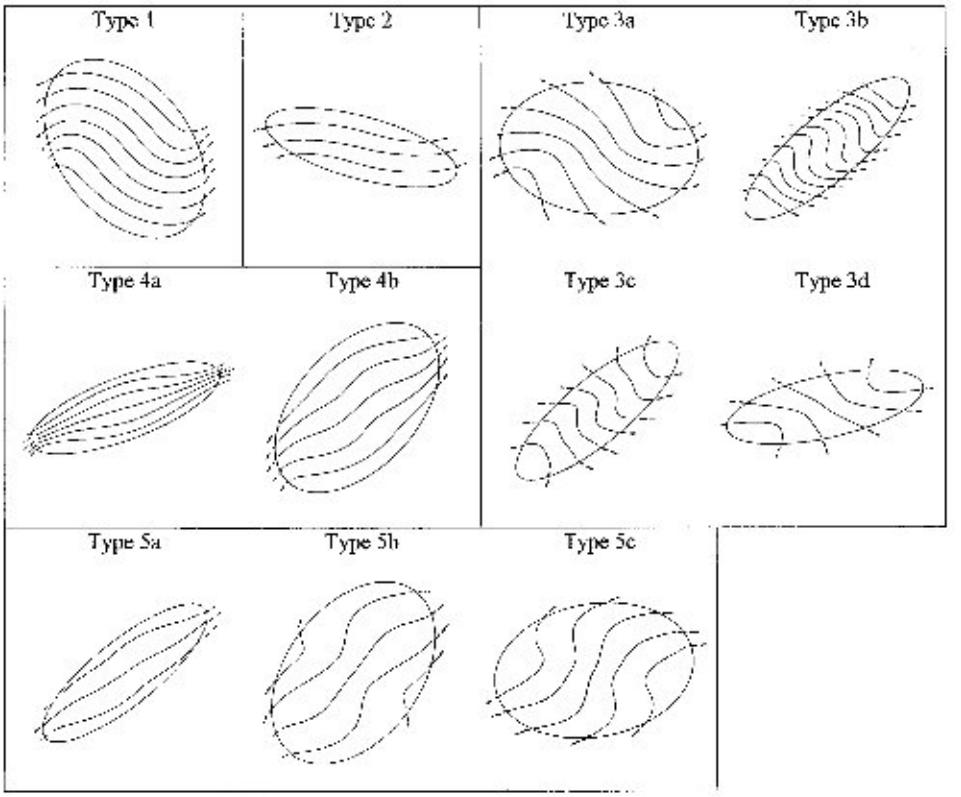

Fig. 26. Types of trail structures in elongate porphyroblasts, obtained from numerical model experiments.

Ji et al. (1997) analyzed development of tensile fractures within non-rectangular, ellipsoidal inclusions. They calculated the tensile stress within the inclusion by considering the traction over the entire surface of the inclusion as opposed to the Ramberg's model (Eq. (11)) that considers the traction only along the long faces of a rectangular inclusion. To calculate the internal tensile stress (σ_{xx}) on a section at right angle to the long axis of the inclusion located at a distance $x$from the center, Ji et al. (1997) have considered the following equation of equilibrium over an infinitesimal element (Fig. 29):

$$r_0(x)^2\frac{\mathrm{d}\sigma(x)}{\mathrm{d}x}+2r_0(x)\sigma(x)\frac{\mathrm{d}r_0(x)}{\mathrm{d}x}+2r_0(x)\tau_0(x)-2\sigma_m r_0(x)\frac{\mathrm{d}r_0(x)}{\mathrm{d}x}=0 \qquad (12)$$

$r_0(x)$ is the radius of the circular cross-section of the inclusion at x, $\sigma(x)$ is the axial tensile stress on the circular cross-section, σ_m is the far field stress in the matrix. $\tau_0(x)$ is the shear stress on the inclusion surface exerted by the matrix. The model of Ji et al. (1997) shows that the initial fracture develops through mid-point fracturing at right angles to the long axis of the inclusion, but the subsequent fractures developing on the smaller, derivative fragments, do not necessarily form at their mid points.

All the above models basically determine the tensile stress within the inclusion and explain only the tensile mode of failure. However, to understand the other modes of failure a different mathematical approach is necessary that analyzes both tensile and compressive stresses within an inclusion. Mandal et al. (2001b) used Griffith's criterion to analyze different modes of intragranular fracturing by calculating principal tensile and compressive stresses within an inclusion.

The tensile and compressive stresses inside an inclusion with its long axis parallel to the bulk

Table 2
Geometrical and kinematic conditions for development of different types of trail patterns in non-spherical porphyroblasts

Simple Shear (S_r = 0)

$\theta = 85°$

$\dot{G}_r$ ↓ / ϕ →	-45°	0°	45°	85°
1.5	*1*	*1*	*1*	*4b*
3	*3a*	*1*	*1*	*4a*

$\theta = 45°$

$\dot{G}_r$ ↓ / ϕ →	-45°	0°	45°	85°
1.5	*3b*	*2*	*2*	*2*
3	*3b*	*1*	*4a*	*2*

$\theta = 0°$

$\dot{G}_r$ ↓ / ϕ →	-45°	0°	45°	85°
1.5	*3b*	*1*	*3a*	*3a*
3	*3c*	*2*	*3c*	*3c*

$\theta = -10°$

$\dot{G}_r$ ↓ / ϕ →	-45°	0°	45°	85°
1.5	*3a*	*3a*	*3a*	*3a*
3	*3c*	*5b*	*3d*	*3d*

$\theta = -45°$

$\dot{G}_r$ ↓ / ϕ →	-45°	0°	45°	85°
1.5	*4b*	*1*	*1*	*1*
3	*5a*	*1*	*3b*	*2*

Combination of Simple Shear and Pure Shear (S_r = 0.25)

$\theta = 85°$

$\dot{G}_r$ ↓ / ϕ →	-45°	0°	45°	85°
1.5	*1*	*1*	*1b*	*1*
3	*3b*	*1*	*1*	*4a*

$\theta = 45°$

$\dot{G}_r$ ↓ / ϕ →	-45°	0°	45°	85°
1.5	*3b*	*4a*	*4a*	*1*
3	*3b*	*1*	*4a*	*1*

$\theta = 0°$

$\dot{G}_r$ ↓ / ϕ →	-45°	0°	45°	85°
1.5	*3b*	*2*	*1*	*1*
3	*3b*	*4a*	*3b*	*3c*

$\theta = -10°$

$\dot{G}_r$ ↓ / ϕ →	-45°	0°	45°	85°
1.5	*3b*	*2*	*3a*	*3a*
3	*3b*	*2*	*3a*	*3c*

$\theta = -45°$

$\dot{G}_r$ ↓ / ϕ →	-45°	0°	45°	85°
1.5	*5b*	*3a*	*5b*	*5b*
3	*5c*	*3a*	*5b*	*5c*

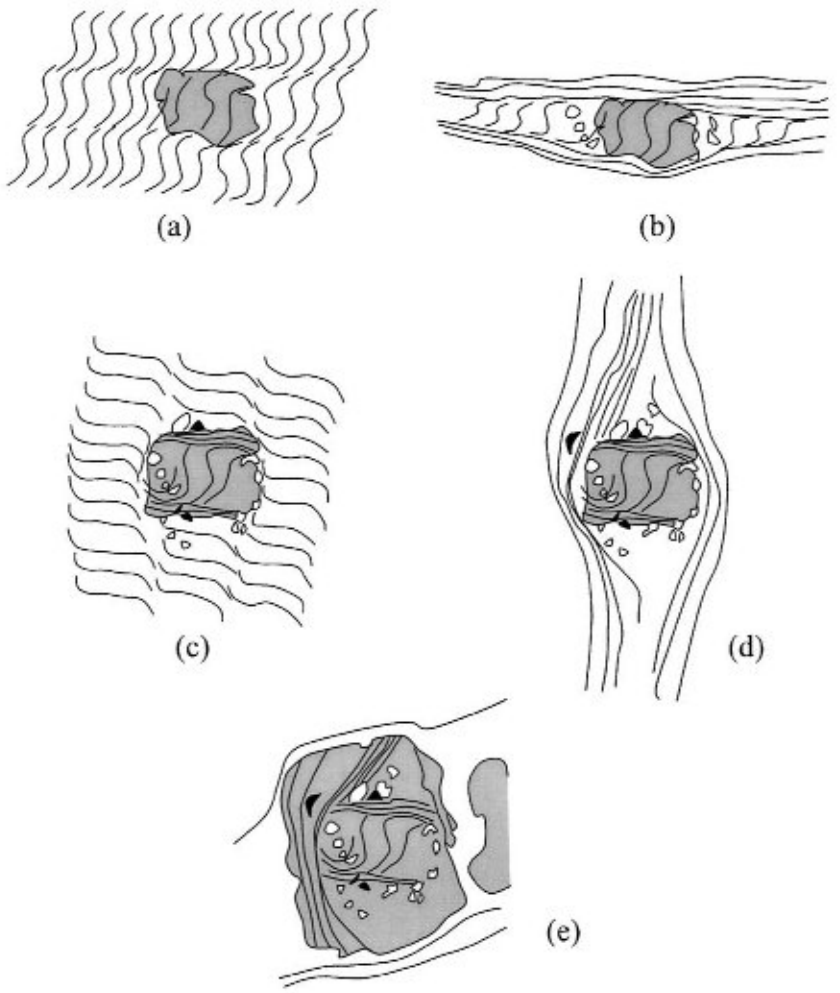

Fig. 27. Development of curved inclusion trails within a porphyroblast that did not rotate during deformation, but entrapped successive stages of crenulation cleavages (after Bell et al., 1998).

extension direction are functions of the axial ratio (R) of inclusion:

$$\sigma_t = -p_o + 2\eta\dot{\varepsilon}(1+R),$$
$$\sigma_c = -p_o - 2\eta\dot{\varepsilon}\left(1+\frac{1}{R}\right) \quad (13)$$

Eq. (13) indicates that the stress inside an inclusion is homogeneous (cf. Eshelby, 1957), and dependent on the aspect ratio (R) of the inclusion at given p_o, η and $\dot{\varepsilon}$values. The shape of the inclusion therefore appears to be a crucial parameter in controlling the fracturing modes, as seen in the experiments. Intragranular fracturing in different modes will occur when the principal tensile and compressive stresses fulfil the Griffith's criterion (Fig. 30):

$$(\sigma_t - \sigma_c)^2 + 8T(\sigma_t + \sigma_c) = 0, \quad \text{if } 3\sigma_t + \sigma_c < 0,$$
$$\sigma_t = T \quad \text{if } 3\sigma_t + \sigma_c > 0, \quad (14)$$

(Jaeger, 1969), where T is the tensile strength of the inclusion. There is a critical value of R (i.e. aspect ratio of inclusion) above which the principal tensile stress (σ_t) satisfies the second condition in Eq. (14), leading to tensile fracturing of the inclusion (Fig. 30).

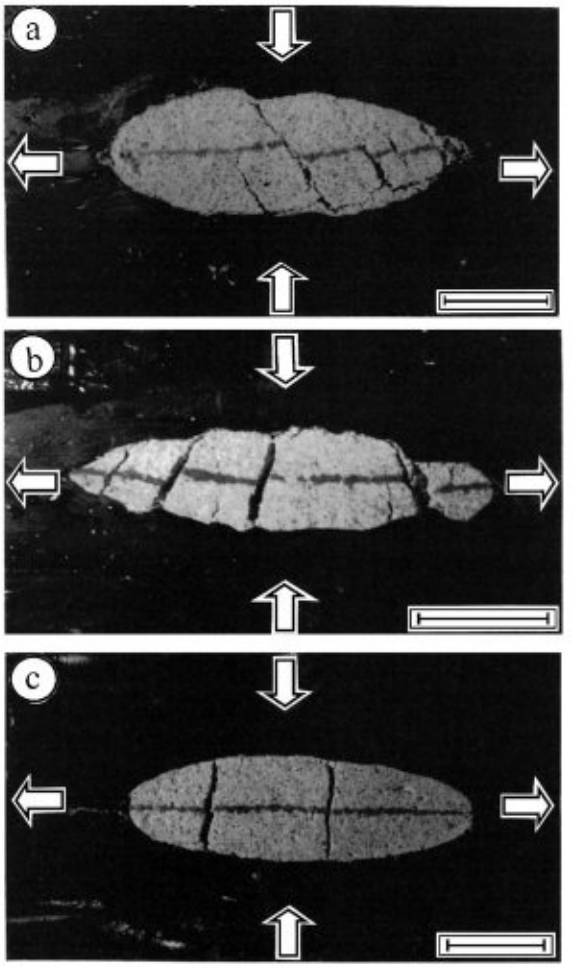

Fig. 28. Different modes of brittle failure of elongate inclusion in physical experiment under pure shear. (a) Shear fracturing (Mode 2a), (b) Extensional-shear fracturing (Mode 2b) and (c) Tensile fracturing (Mode 1). Scale bars: 2 cm.

For other values of R less than the critical value, brittle failure will take place either by shear or extensional shear fracturing as defined in the first condition of Eq. (14), and there is also another critical aspect ratio that marks the transition between Mode 2a and Mode 2b satisfying the stress condition: $\sigma_t - \sigma_c = 5.7T$.

Similarly, the different critical aspect ratios delimiting the conditions for different modes of failure can be determined for different orientations of the inclusion with respect to the bulk extension direction, and the results so obtained can be utilized to show fields of different failure modes in a $R-\phi$ space (Fig. 31).

9. Concluding remarks

Presence of rigid or stiff inclusions such as large mineral grains (porphyroblasts or porphyroclasts), xenoliths, pebbles, etc. within a rock body imparts a mechanical heterogeneity in the system. During deformation, the inclusions perturb the flow of matrix leading to a heterogeneous strain field around them, which is manifested in the complex distortions of passive foliation around rigid inclusions. The other varieties of micro- to macro-scale structures that develop under the influence of the heterogeneous strain field around the inclusions include strain shadow, porphyroclast tails, porphyroblast inclusion trails and intragranular fractures. The development of these structures in relation to the heterogeneous flow around inclusions is currently being intensively studied in structural geology for their precise and proper application in the kinematic analysis of deformed rocks.

In addition to matrix rheology (e.g. elastic or Newtonian or non-Newtonian viscous) the other factors controlling the nature of strain heterogeneity around an inclusion include shape and orientation of inclusion and the vorticity of bulk deformation. For example, equant inclusions develop flow patterns characterized by harmonic closed particle paths with eye-shaped or bow-tie-shaped separatrix. When the inclusion is inequant in shape, the flow patterns become much more complex, reflecting an unsteady state of motion and showing a wide spectrum of particle paths. Consequently, structures, such as strain shadows and drag patterns of passive foliations etc., forming around inclusions of different shapes and orientations, are of contrasting nature even if they develop under the same bulk kinematic condition. It is therefore essential to take into account the effect of inclusion geometry while utilizing such structures for the kinematic analysis of deformed rocks.

Under favourable conditions, inclusions may undergo size-reduction (e.g. porphyroclasts) forming a deformable mantle around the rigid core. The mantle subsequently experiences deformation under the heterogeneous strain field induced by the rigid core, and gives rise to different types of tail structures. The rate of size-reduction is the prime physical parameter in determining the mantle geometry of porphyroclasts, as revealed from analog and numerical model experi-

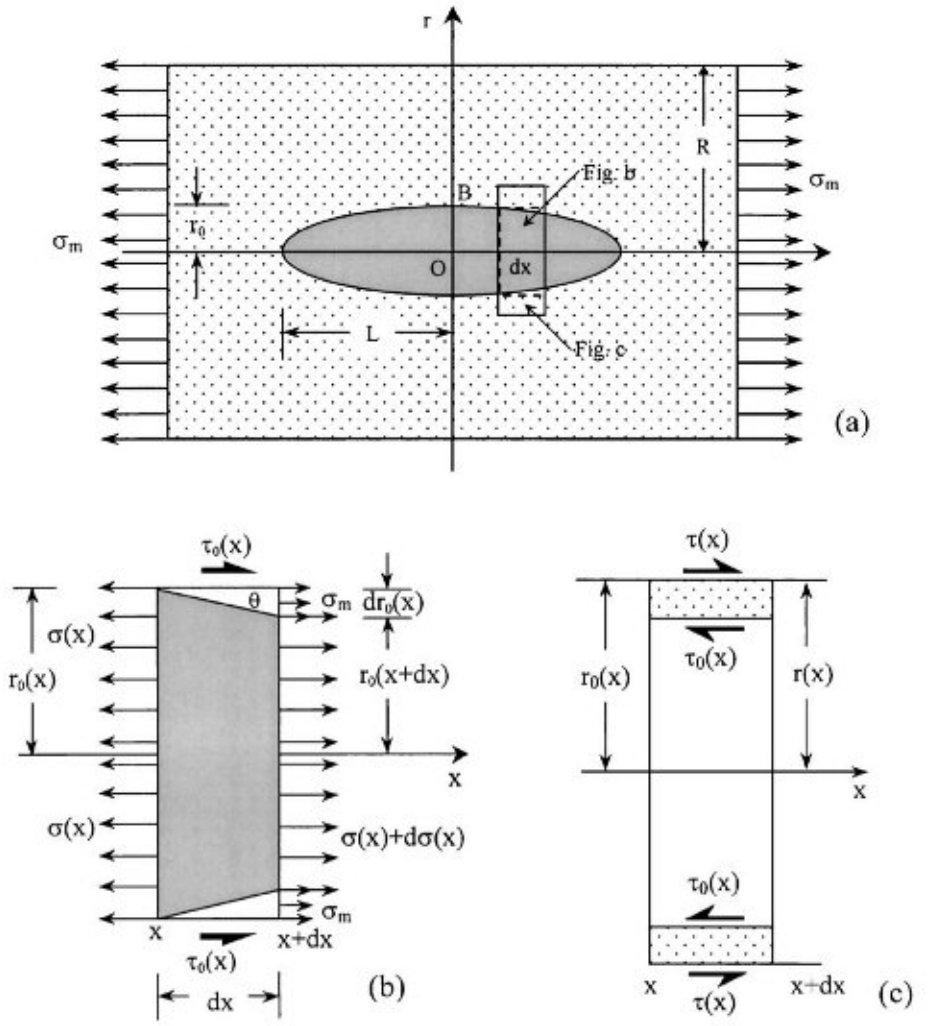

Fig. 29. Considerations of dynamic settings for the mechanical equilibrium analysis in shear-lag model (after Ji et al., 1997).

ments by Passchier and Simpson (1986) and several workers later on. Under a constant size-reduction rate, the variation in mantle structures of porphyroclasts may result due to several other factors, such as shape and orientation of porphyroclasts, coupling factor between porphyroclast and matrix, matrix rheology (Newtonian or non-Newtonian) and kinematical vorticity number W_k of the bulk deformation, which govern the heterogeneous strain field around an inclusion.

Synkinematically rotating porphyroblasts growing over a pre-existing, passive foliation during a single phase of deformation and metamorphism are characterized by curved or spiral inclusion trails. Earlier workers (e.g. Ghosh and Ramberg, 1978) attempted to explain the inclusion trail patterns by considering the relative rotation rates of porphyroblast and the external foliation. It is evident from different models discussed in this review that this kind of analytical approach is difficult to apply in explaining some complex inclusion patterns that essentially reflect a heterogeneous strain field around the growing porphyroblasts. To summarize, the application of hydrodynamic theories describing the flow field around rigid inclusions is essential for analyzing the minute details of inclusion trail patterns in syntectonic por-

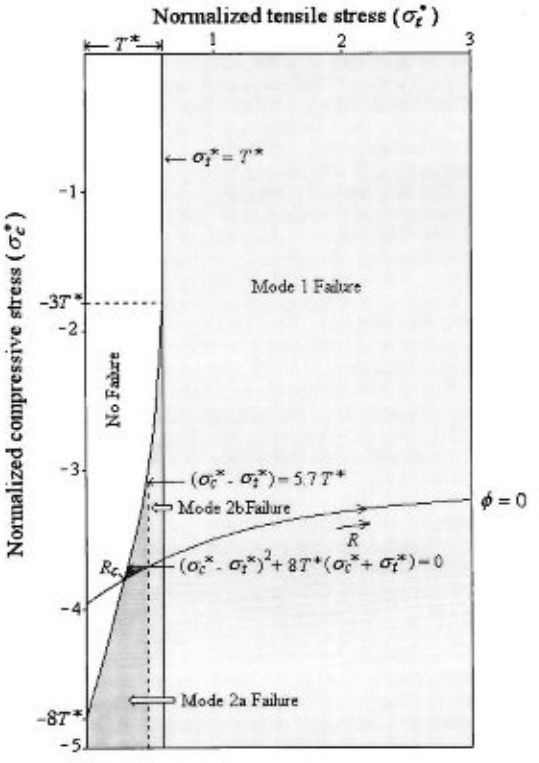

Fig. 30. Fields of different failure modes in the (σ_t^*, σ_c^*) space where σ_t^* and σ_c^* are the principal stresses in the inclusions as normalized by the bulk flow stress ($2\eta\dot{\varepsilon}$). The failure curve obtained from Griffith's failure criterion separates the stable (unshaded) and unstable fields (shaded). The arrowed line shows the variation of principal tensile and compressive stresses within an inclusion with increasing aspect ratio (R). $\phi = 0$ signifies that the long axis of the inclusion is parallel to the bulk extension direction. The value of R at the point of intersection of the arrowed line with the failure curve represents the critical aspect ratio (R_c) for the commencement of fracturing within the inclusion.

phyroblasts. In multiply deformed terrains the interpretation of inclusion trail structures is obviously much more difficult, because the porphyroblast structures may not actually represent a single, non-coaxial deformations, and curved inclusion trails may develop even within porphyroblasts that did not rotate during deformation. Use of curved inclusion trails for the analysis of rotationality of deformation should therefore be exercised with caution.

Different continuum models have been applied in structural geology, as discussed in this review, in order to investigate the structural development in relation to the strain field around rigid or stiff inclusions within deformed rocks. In spite of a significant advancement there is still some lacuna in this field of study. Most of the existing models are based on a system where the inclusions are in dilute suspension and are mechanically non-interacting. But rock systems often contain inclusions in a high volume density. Experimental studies indicate that inclusions in such a situation generally interact with one another mechanically, developing heterogeneous strain fields different from those around non-interacting inclusions (Ildefonse et al., 1992). Understandably, new theoretical and numerical models are required in this line of work in order to investigate the progressive development of structures in mechanically interacting inclusion systems. In addition, the application of hydrodynamic models on three-dimensions would be more effective. The task is certainly difficult because the kinematics of rigid inclusions (Passchier, 1987) as well as the velocity functions defining the flow field in three-dimension is somewhat complex. However, by applying different computer softwares, which are now emerging rapidly, such hurdles can be surmounted (e.g. Jezek et al., 1999).

Barring a few, existing continuum models mostly deal with Newtonian rheology of the matrix. To our

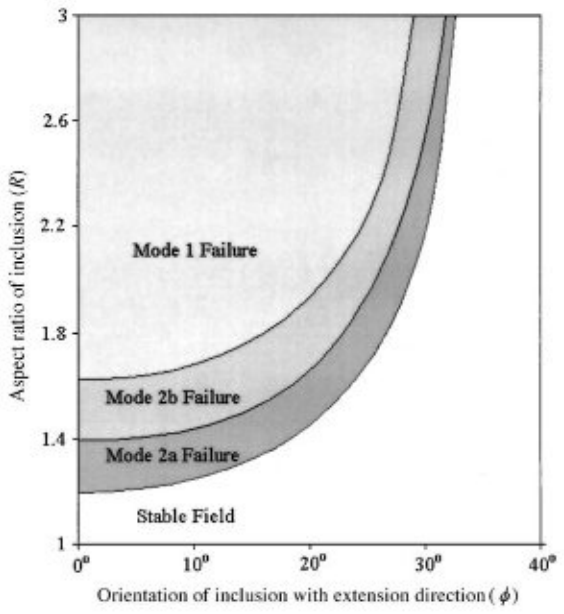

Fig. 31. Fields for the three modes of failure (under pure shear) in the $R-\phi$ space.

knowledge, there is hardly any analytical solution of the velocity field around rigid inclusions (inequant shape in particular) for a non-Newtonian matrix. There is a scope to extend the study considering nonlinear rheology of the matrix.

Acknowledgements

We wish to thank Prof. T.H. Bell and an anonymous reviewer for their critical comments that have improved the manuscript significantly. The present work was carried out under a project of Department of Science and Technology (India), sanctioned to NM. SKS is grateful to the University Grants Commission, India for the Research Fellowship. CC acknowledges the infrastructural facilities provided by the Indian Statistical Institute, Calcutta.

References

Beam, E.C., 1996. Modeling growth and rotation of porphyroblasts and inclusion trails. In: De Paor, D.G. (Ed.), Structural Geology and Personal Computers. Computer Methods in the Geosciences, vol. 15. Pergamon, London, pp. 247–258.

Bell, T.H., 1985. Deformation partitioning and porphyroblast rotation in metamorphic rocks: a radical reinterpretation. J. Metamorph. Geol. 3, 109–118.

Bell, T.H., Hickey, K.A., 1997. Distribution of pre-folding linear indicators of movement direction around the Spring Hill Synform, Vermont: significance for mechanism of folding in this portion of the Appalachians. Tectonophysics 274, 275–294.

Bell, T.H., Johnson, S.E., 1989. Porphyroblast inclusion trails: the key to orogenesis. J. Metamorph. Geol. 7, 279–310.

Bell, T.H., Rubenach, M.J., 1986. Crenulation cleavage development—evidence for progressive, bulk inhomogeneous shortening from "millipede" microstructures in the Robertson River Metamorphics. Tectonophysics 68, T9–T15.

Bell, T.H., Forde, A., Hayward, N., 1992. Do smoothly curving, spiral-shaped inclusion trails signify porphyroblast rotation? Geology 20, 59–62.

Bell, T.H., Hickey, K.A., Wang, J., 1997. Spiral and staircase inclusion trail axes within garnet and staurolite pophyroblasts from schists of the Bolton syncline, Connecticut: timing of porphyroblast growth and the effects of fold development. J. Metamorph. Geol. 15, 467–478.

Bell, T.H., Hickey, K.A., Upton, G.J.G., 1998. Distinguishing and correlating multiple phases of metamorphism across a multiply deformed region using the axes of spiral, staircase and sigmoidal inclusion trails in garnet. J. Metamorph. Geol. 16, 767–794.

Bjornerud, M.G., 1989. Mathematical model for folding of layering near rigid inclusions in shear deformation. J. Struct. Geol. 11, 245–254.

Bjornerud, M.G., Zhang, H., 1994. Rotation of porphyroblasts in non-coaxial deformation: insights from computer simulations. J. Metamorph. Geol. 12, 135–139.

Bjornerud, M.G., Zhang, H., 1995. Flow mixing inclusion matrix coherent mantle growth and the development of porphyroclast tails. J. Struct. Geol. 17, 1347–1350.

Cox, H.L., 1952. The elasticity and strength of paper and other fibrous materials. Br. J. Appl. Phys. 3, 72–79.

Eshelby, J.D., 1957. The determination of the elastic field of an ellipsoidal inclusion, related problems. Proc. R. Soc. Lond. A241, 376–396.

Eshelby, J.D., 1959. The elastic field outside an ellipsoidal inclusion. Proc. R. Soc. Lond. A252, 561–569.

Ferguson, C.C., 1979. Rotations of elongate rigid particles in slow non-Newtonian flows. Tectonophysics 60, 247–262.

Fernandez, A., 1987. Preferred orientation developed by rigid markers in two-dimensional simple shear strain: a theoretical and experimental study. Tectonophysics 136, 151–158.

Freeman, B., 1985. The motion of rigid ellipsoidal particles in slow flows. Tectonophysics 113, 163–183.

Gay, N.C., 1968. Pure shear and simple shear deformation of inhomogeneous viscous fluids. 1. Theory. Tectonophysics 5, 211–234.

Ghosh, S.K., 1975. Distortion of planar structures around rigid spherical bodies. Tectonophysics 28, 185–208.

Ghosh, S.K., Ramberg, H., 1976. Reorientation of inclusions by combination of pure shear and simple shear. Tectonophysics 34, 1–70.

Ghosh, S.K., Ramberg, H., 1978. Reversal of spiral direction of inclusion-trials in paratectonic pophyroblast. Tectonophysics 52, 83–97.

Ghosh, S.K., Sengupta, S., 1973. Compression and simple shear test models with rigid and deformable inclusions. Tectonophysics 17, 133–175.

Gray, N.H., Busa, M.D., 1994. The three-dimensional geometry of simulated porphyroblast inclusion trails: inert marker, viscous-flow models. J. Metamorph. Geol. 12, 575–587.

Hancock, P.L., 1985. Brittle microtectonics: principles and practices. J. Struct. Geol. 7, 437–457.

Hickey, K.A., Bell, T.H., 1999. Behaviour of rigid inclusions during deformation and metamorphism: a test using schists from the Bolton syncline, Connecticut, USA. J. Metamorph. Geol. 17, 211–228.

Hippertt, J.F.N., 1993. "V"-pull apart microstructures: a new shear sense indicator. J. Struct. Geol. 15, 1393–1404.

Hobbs, D.W., 1967. The formation of tension joints in sedimentary rocks: an explanation. Geol. Mag. 104, 550–556.

Ildefonse, B., Mancktelow, N.S., 1993. Deformation around rigid particle: influence of slip at the particle/matrix interface. Tectonophysics 221, 345–359.

Ildefonse, B., Sokoutis, D., Mancktelow, N.S., 1992. Mechanical interactions between rigid particles in a deforming ductile matrix. Analogue experiments in simple shear flow. J. Struct. Geol. 14, 1253–1266.

Jaeger, J.C., 1969. Elasticity, Fracture and Flow. Methuen, London.

Jeffery, G.B., 1922. The motion of ellipsoidal particles immersed in a viscous fluid. Proc. R. Soc. Lond. A 120, 161–179.

Jezek, J., Schulmann, K., Segeth, K., 1996. Fabric evolution of rigid inclusions during mixed coaxial and simple shear flows. Tectonophysics 257, 203–221.

Jezek, J., Saic, S., Segeth, K., Schulmann, K., 1999. Three-dimensional hydrodynamical modelling of viscous flow around a rotating ellipsoidal inclusion. Comput. Geosci. 25, 547–558.

Ji, S., Saruwatari, K., 1998. A revised model for the relationship between joint spacing and layer thickness. J. Struct. Geol. 20, 1495–1508.

Ji, S., Zhao, P., 1993. Location of tensile fracture within rigid–brittle inclusions in a ductile flowing matrix. Tectonophysics 220, 23–31.

Ji, S., Zhao, P., Saruwatari, K., 1997. Fracturing of garnet crystals in anisotropic rocks during uplift. J. Struct. Geol. 19, 603–620.

Johnson, S.E., Bell, T.H., 1996. How useful are 'millipede' and other similar porphyroblast microstructures for determining syn-metamorphic deformation histories? J. Metamorph. Geol. 14, 15–28.

Johnson, S.E., Moore, R.R., 1996. De-bugging the "millipede" porphyroblast microstructure: a serial thin-section study and 3-D computer animation. J. Metamorph. Geol. 14, 3–14.

Kenkmann, T., Dresen, G., 1998. Stress gradients around porphyroclasts: palaeopiezometric estimates and numerical modelling. J. Struct. Geol. 20, 163–173.

Lamb, H., 1932. Hydrodynamics. Cambridge University Press, Cambridge.

Lloyd, G.E., Ferguson, C.C., 1981. Boudinage structure — some new interpretations based on elastic–plastic finite element simulations. J. Struct. Geol. 3, 117–129.

Lloyd, G.E., Ferguson, C.C., Reading, K., 1982. A stress-transfer model for the development of extension fracture boudinage. J. Struct. Geol. 4, 355–372.

Mandal, N., Banerjee, S., 1987. Rotation rate versus growth rate of syntectonic porphyroblasts: the controlling parameter of the shape of the inclusion trail. Tectonophysics 136, 165–169.

Mandal, N., Chakraborty, C., 1990. Strain fields and foliation trajectoriesaround pre-, syn- and post-tectonic plutons in coaxially deformedterrains. Geol. J. 25, 19–33.

Mandal, N., Deb, S.K., Khan, D., 1994. Evidence of a non-linear relationship between fracture spacing and layer thickness. J. Struct. Geol. 16, 1275–1281.

Mandal, N., Chakraborty, C., Samanta, S.K., 2000a. Boudinage in multilayered rocks under layer-normal compression: a theoretical analysis. J. Struct. Geol. 22, 373–382.

Mandal, N., Samanta, S.K., Chakraborty, C., 2000b. Progressive development of mantle structures around elongate porphyroclasts: insights from numerical models. J. Struct. Geol. 22, 993–1008.

Mandal, N., Samanta, S.K., Chakraborty, C., 2001a. Numerical modeling of heterogeneous flow fields around rigid objects with special reference to particle paths, strain shadows and foliation drag. Tectonophysics 330, 177–194.

Mandal, N., Chakraborty, C., Samanta, S.K., 2001b. Controls on the failure mode of brittle inclusions hosted in a ductile matrix. J. Struct. Geol. 23, 51–66.

Masuda, T., Ando, S., 1988. Viscous flow around a rigid spherical body: a hydrodynamical approach. Tectonophysics 148, 337–346.

Masuda, T., Kuriyama, M., 1988. Successive "mid-point" fracturing during microboudinage: an estimate of the stress–strain relation during a natural deformation. Tectonophysics 147, 171–177.

Masuda, T., Mizuno, N., 1995. Deflection of pure shear viscous flow around a rigid spherical body. J. Struct. Geol. 17, 1615–1620.

Masuda, T., Mizuno, N., 1996a. Deflection of non-Newtonian simple shear flow around a rigid cylindrical body by the finite element method. J. Struct. Geol. 18, 1089–1100.

Masuda, T., Mizuno, N., 1996b. Computer modeling mantled porphyroclasts in Newtonian and non-Newtonian simple shear viscous flows. J. Struct. Geol. 18, 1487–1491.

Masuda, T., Mochizuki, S., 1989. Development of snowball structures: numerical simulation of inclusion trails during synkinematic porphyroblast growth in metamorphic rocks. Tectonophysics 170, 141–150.

Masuda, T., Michibayashi, K., Ohata, H., 1995. Shape preferred orientation of rigid particles in a viscous matrix: reevaluation to determine parameters of ductile deformation. J. Struct. Geol. 17, 115–129.

Michibayashi, K., 1996. The role of intragranular fracturing on grain size reduction in feldspar during mylonitization. J. Struct. Geol. 18, 17–25.

Mitra, S., 1978. Microscopic deformation mechanisms and flow laws in quartzites within the South Mountain anticline. J. Geol. 86, 129–152.

Muskhelishvilli, N.I., 1953. Some Basic Problems of the Mathematical Theory of Elasticity P. Noordhoff, Groningen, Holland.

Oertel, G., 1965. Slow viscous flow of an incompressible suspension. J. Eng. Mech. Div., ASCE 91, 145–154.

Passchier, C.W., 1987. Stable positions of rigid inclusions in non-coaxial flow: a study in vorticity analysis. J. Struct. Geol. 9, 679–690.

Passchier, C.W., 1994. Mixing in flow perturbations: a model for development of mantle porphyroclasts in mylonites. J. Struct. Geol. 16, 733–736.

Passchier, C.W., Simpson, C., 1986. Porphyroclast systems as kinematic indicators. J. Struct. Geol. 8, 831–844.

Passchier, C.W., Sokoutis, D., 1993. Experimental modeling of mantled porphyroclasts. J. Struct. Geol. 15, 895–910.

Passchier, C.W., Trouw, R.A.J., 1996. Microtectonics Springer, Berlin.

Passchier, C.W., Trouw, R.A.J., Zwart, H.J., Vissers, R.L.M., 1992. Porphyroblast rotation: eppur si move? J. Metamorph. Geol. 10, 283–294.

Passchier, C.W., ten Brink, C.E., Bons, P.D., Sokoutis, D., 1993. δ inclusions as a gauge for stress sensitivity of strain rate in mylonites. Earth Planet. Sci. Lett. 120, 239–245.

Pennacchioni, G.P., Fasolo, L., Cecchi, M.M., Salasnich, L., 2000. Finite-element modeling of simple shear flow in Newtonian and non-Newtonian fluids around circular rigid particle. J. Struct. Geol. 22, 683–692.

Pollard, D.D., Segall, P., 1987. Theoretical displacements and stresses near fractures in rocks with applications to faults, joints,

veins, dikes, and solution surfaces. In: Atkinson, B.K. (Ed.), Fracture Mechanics of Rocks. Academic Press, London, pp. 277–349.

Powell, C.McA., Vernon, R.H., 1979. Growth and rotation history of garnet porphyroblasts with inclusion spirals in Karakoram Schist. Tectonophysics 54, 25–43.

Ramberg, H., 1955. Natural and experimental boudinage and pinch-and-swell structures. J. Geol. 63, 512–526.

Ramsay, J.G., Huber, M.I., 1987. The Techniques of Modern Structural Geology. Folds and Fractures, vol. 2. Academic Press, London.

Rast, N., 1958. Metamorphic history of the Schichallion complex. Trans. R. Soc. Edinburgh 63 (2), 413–432.

Reed, L.J., Tryggvason, E., 1974. Preferred orientation of rigid particles in a viscous matrix deformed by pure shear and simple shear strain. Tectonophysics 24, 85–98.

Rosenfeld, J.L., 1970. Rotated garnets in metamorphic rocks. Spec. Pap. Geol. Soc. Am.

Samanta, S.K., Mandal, N., Chakraborty, C., Majumder, K., 2001. Simulation of inclusion trail patterns of synkinematic porphyroblasts. Comput. Geosci., (in press).

Schoneveld, C., 1977. A study of some typical inclusion patterns in strongly paracrystalline rotated garnets. Tectonophysics 39, 453–471.

Simpson, C., De Paor, D., 1993. Strain and kinematic analyses in general shear zones. J. Struct. Geol. 15, 1–20.

Spry, A., 1969. Metamorphic Textures Pergamon, Oxford.

Stewart, L.K., 1997. Experimental investigation of the effects of fluid heterogeneity upon the motion of rigid ellipsoidal inclusions during bulk inhomogeneous shortening. J. Struct. Geol. 19, 1231–1243.

ten Brink, C., Passchier, C.W., 1995. Modeling of mantled porphyroclasts using non-Newtonian rock analogue materials. J. Struct. Geol. 17, 131–146.

ten Brink, C.E., Bons, P.D., Passchier, C.W., 1993. Approximate stream functions for flow around rigid inclusions in shear zones. Abstract Supplement No. 2 to Terra Nova, pp. 5–35.

Turcotte, D., Schubert, G., 1982. Geodynamics: Applications of Continuum Physics to Geological Problems. Wiley, New York.

Van Der Driessche, J., Brun, J.P., 1987. Rolling structures at large shear strain. J. Struct. Geol. 9, 691–704.

Zwart, H.J., 1960. Relations between folding and metamorphism in the central Pyrenees. Geol. Mijnbouw 39d, 163.